Arabian Journal for Science and Engineering
https://doi.org/10.1007/s13369-026-11357-0

RESEARCH ARTICLE-PHYSICS

Deconvoluting Grain and Grain Boundary Responses in Ag-Substituted Co-Ni-Zn-Cu Nanospinel Ferrites: A Comprehensive Impedance Spectroscopy Analysis

A. Mihmanli[1] · M. A. Almessiere[2,3] · B. Ünal[4] · A. Baykal[5] · A. Korkmaz Demir[6] · M. A. Gondal[7,8] · E. Mojtahedi[9] · S. E. Shirsath[10]

Received: 23 January 2026 / Accepted: 14 April 2026

Abstract

$Co_{0.25}Ni_{0.25}Zn_{0.25}Cu_{0.25}Ag_xFe_{2-x}O_4$ ($0.00 \leq x \leq 0.10$) nanospinel ferrites (Ag → CoNiZnCu ($x \leq 0.10$) NSFs) have been synthesized via a one-pot sol–gel method. XRD analysis was applied to prove the phase formation for each product. The morphologies were confirmed via SEM/TEM. This study introduced a detailed analysis of the electrical and dielectric properties of ion-substituted spinel ferrites. AC/DC conductivity and complex impedance spectroscopy were both used to understand how substitution of Ag^+ affects the charge-transport properties of these (NSFs). The unsubstituted NSF ($x = 0.00$) had very high resistivity (GΩ range) and was found to be mainly affected by one process of relaxation that occurred due to high resistive grain boundaries. After substitution with Ag, the DC conductivity increased dramatically by several orders of magnitude, which correlated with a massive reduction in resistance of the grain boundaries. The overall electrostatic and dielectric properties of these NSFs changed drastically with Ag^+ ion substitution as well; this change was due to the presence of the effect known as colossal permittivity ($\epsilon' > 104$), which is explained by the Maxwell–Wagner theory of interfacial polarization. All types of analysis (using both the complementary impedance and electric modulus formalisms, including Nyquist plots) proved that by separating the different electrical responses from the grains and grain boundaries of the substituted NSFs, these materials are heterophase-natured. Therefore, it can be concluded that Ag + ion substitution is a very effective way to tune the properties of grain boundaries, resulting in a measurable difference in the total electrical/dielectric response of the NSFs.

Keywords Dielectric properties · Conductivity · Nyquist study · Multielement spinel ferrites

✉ A. Baykal
abdulhadibaykal@aydin.edu.tr

[1] Faculty of Dentistry, Gelişim University, 34310, Avcılar Istanbul, Turkey

[2] Department of Physics, College of Science, Imam Abdulrahman Bin Faisal University, P.O. Box 1982, 31441 Dammam, Saudi Arabia

[3] Department of Biophysics, Institute for Research and Medical Consultations (IRMC), Imam Abdulrahman Bin Faisal University, P.O. Box 1982, 31441 Dammam, Saudi Arabia

[4] Department of Electrical and Electronics Engineering, Faculty of Engineering and Architecture, İstanbul Gelisim University, 34310, Avcılar Istanbul, Turkey

[5] Food Engineering Department, Istanbul Aydin University, 34295 Istanbul, Turkey

[6] Gastronomy and Culinary Arts Department, Faculty of Fine Arts, Istanbul Aydin University, 34295 Istanbul, Turkey

[7] Department of Chemistry, Istanbul Medeniyet University, 34700, Uskudar Istanbul, Turkey

[8] Laser Research Group, Department of Physics & Interdisciplinary Research Center for Hydrogen Technologies, King Fahd University of Petroleum &Minerals, KFUPM, Box 5040, 31261 Dhahran, Dammam, Saudi Arabia

[9] K. A. CARE Energy Research and Innovation Center, King Fahd University of Petroleum & Minerals, KFUPM, Box 5040, 31261 Dhahran, Dammam, Saudi Arabia

[10] Department of Physics, Vivekanand College, r, Chhatrapati Sambhajinaga, MS 431001, India

Published online: 28 April 2026

1 Introduction

Ferrites represent an important class of ferrimagnetic NSFs with wide technological relevance and are commonly classified as garnet ($M_3Fe_5O_{12}$), spinel (MFe_2O_4), magneto plumbite ($MFe_{12}O_{19}$), and orthoferrites ($MFeO_3$), where M denotes a divalent metal cation (e.g., Mg^{2+}, Ni^{2+}, Zn^{2+}). Among ferrites, spinel ferrites attract strong technological interest due to their high magnetization, stability, tunable composition, low dielectric loss, low coercivity, low cost, and wide band gap [1, 2]. Spinel ferrite properties are influenced by variables such as synthesis conditions, electronic configuration, stoichiometry, particle size, and substituent choice. Synthesis approaches include hydrothermal, sol–gel, microemulsion, sol–gel auto combustion, co-precipitation, thermolysis, and microwave-assisted methods [3].

Spinel ferrites, owing to their unique properties, are widely used for various applications such as microwave absorbers, memory and data storages, magnetic nanofluids, humidity and gas sensors, targeted drug delivery, catalysis, supercapacitors, magnetic storages and switches, recording media, microelectronics, electronic filter, pharmaceuticals, cancer treatment, photo magnetics, magnetic bulk and transformer cores, MRI, magnetostrictive vibrator, electromagnetic shielding, lithium ion batteries, high-frequency power devices, radar-absorbing NSFs, magnetic hyperthermia therapy, and medical diagnostics [2, 4–6]**.**

Spinel ferrites are cubic ferrites in which cations occupy both octahedral (B) and tetrahedral (A) sites of the oxygen lattice. Their electrical and magnetic properties arise from A–B super exchange interactions. Substituting with M^{2+} or M^{3+} ions or rare earth elements **(REs)** redistribute cations between these sites, altering super exchange and strongly affecting saturation magnetization, the coercivity, blocking temperature, and electrical resistance [7–9].

The impact of multielement substituting and cation distribution on the magnetic, electrical, and dielectric features of spinel ferrites has been widely documented [10, 11].

Among various substituents, Ag^{2+}-substituted nanospinel ferrites are increasingly important for applications in catalysis, sensing, energy storage, magnetic fluids, biomedical drug delivery, and information storage [12]. Silver nanoparticles' distinctive physical and chemical properties may considerably promote and boost electrochemical performance and Ag^{+} ions incorporated into the crystalline spinel network may improve its efficiency, durability, and long-term chemical stability in the face of environmental fluctuations [13]. Fei et al. stated that chemical silver plating synergistically enhances the contribution of interfaces and defects in the Ni-Zn-Nd spinel ferrite-based electromagnetic wave absorbing material, and the introduction of chemically plated **Ag NPs** weakens the magnetic properties of the composites, but it also introduces lattice defects and a dielectric loss mechanism dominated by polarization loss [14]. In $Cd_{0.5}Cu_{0.5-x}Ag_xFe_2O_4$, Ag^{+} substitution altered the A/B-site distribution, caused lattice shrinkage, induced paramagnetism at $x \geq 0.4$, and reduced magnetization by weakening A–B super exchange in magnetic catalysts [15]. In sol–gel-derived $CoAg_xFe_{2-x}O_4$ ($x = 0.0$—0.4), Ag^{+} substitution increased the lattice parameters, decreased rigidity, and modified dielectric behavior. Cole–Cole plots with single semicircles indicated grain boundary-dominated conduction [16]**. Ag^{+}ion substitution into $CoFe_2O_4$** ferrites enhanced the lattice parameters, improved the antibacterial properties, and shifted the magnetism from ferromagnetic to superparamagnetic, linked to particle size and/or anisotropy effects [17]. Rathod et al. [18] demonstrated as Ag^{+} amount at $CuFe_{2-x}Ag_{x,}O_4$ ferrites increased the saturation magnetization of NSFs decreased. Ag substitution in ultrasound-assisted sol–gel $Zn_{0.5}Co_{0.5-x}Ag_{2x}Fe_2O_4$ for cancer application decreased the coercivity and magnetization [19]. Ag^{2+} ion substitution in Zn–Cu ferrites ($Zn_{0.5}Cu_{(0.5-x)}Ag_xFe_2O_4$) produced 50–65 nm crystallites and enhanced dielectric/magnetic properties while maintaining ferromagnetism [12].

Aydi et al. [20] studied on conduction mechanism and dielectric relaxation in $LiMg_{0.5}Fe_2O_4$ spinel ferrite: a temperature- and frequency-dependent complex impedance study. Defect-engineered charge-transport and dielectric relaxation in In/Se co-substituted CoNi spinel ferrite nanoparticles by sonochemical route search by Almeesiere research group [21]. In another study, the same group studied on the role of Al^{3+} ion substitution in modulating conductivity and interfacial polarization in CoNiCuZn spinel ferrite [22]. The effect of Cd^{2+} and Nd^{3+} ions substitution on dielectric and impedance properties of $Ni_xCd_{1-x}Nd_yFe_{2-y}O_4$ ($0 \leq x \leq 1.0$) spinel ferrites nanoferrites for high-frequency applications was studied by Murthy et al. [23]. Ashiq et al. [25] investigated the dielectric, impedance, and electric modulus properties of lanthanum-doped zinc spinel ferrite ($ZnLa_xFe_{2-x}O_4$) nanomaterials. The complex impedance spectroscopic analysis of charge-transport and relaxation mechanism in $Co_{0.5}Cu_{0.5}Fe_2O_4$ nanoferrites was searched by Rani et al. [25].

While silver (Ag) incorporation has been briefly studied in binary and ternary ferrite systems such as $CoFe_2O_4$, $NiFe_2O_4$, and $CuFe_2O_4$, research has predominantly focused on how it alters lattice parameters, magnetic properties, and defect-driven interfacial polarization [18, 26, 27]. For instance, doping $CoFe_2O_4$ with Ag typically shifts conduction to the grain boundaries and alters dielectric behavior, whereas in $NiFe_2O_4$, it boosts both conductivity and dielectric response. In Ag-plated Ni–Zn–Nd systems, the primary effects are interfacial; defects and heterojunctions amplify polarization losses rather than altering the internal transport mechanisms of the spinel grains. Similarly, investigations

into Ag-doped Co–Zn and $CuFe_2O_4$ ferrites have largely been confined to structural and optical characterizations or specific application testing [18, 26–28].

Noticeably absent from the literature, however, is a rigorous, quantitative impedance-spectroscopic analysis of an Ag-substituted multication spinel, specifically the Co–Ni–Zn–Cu system. This gap is highly significant. Compared to simple binary hosts, multielement spinel ferrites feature intense cation-site competition and generate far more intricate grain and grain-boundary transport networks [29]. Previous studies on multielement spinels confirm that compositional complexity fundamentally alters site occupancy and microstructural development, making the Ag-substituted $Co_{0.25}Ni_{0.25}Zn_{0.25}Cu_{0.25}Ag_xFe_{2-x}O_4$ host an essential target for independent investigation.

To address this, our study outlines the synthesis of $Co_{0.25}Ni_{0.25}Zn_{0.25}Cu_{0.25}Ag_xFe_{2-x}O_4$ (where x ranges from 0.00 to 0.10) nanospinel ferrites using a one-pot sol–gel method. We systematically evaluate the impact of Ag^+ substitution on the material's structural evolution, cation distribution, AC/DC conductivity, and activation energy. Furthermore, we provide a thorough analysis of its dielectric properties and electric modulus. Crucially, this represents the first comprehensive effort to map Ag^+ substitution within this multielement host utilizing impedance-based deconvolution to clearly separate grain and grain-boundary responses.

The objective of current study is to synthesize Ag → CoNiZnCu ($x \leq 0.10$) NSFs with a sol–gel method and evaluate the effect of Ag substitution on the structure, cation distribution, electrical, and dielectric properties of NSFs. We aimed to replace Fe^{3+} ions by non-magnetic Ag^+ ions so as to tune the electrical and dielectric properties of host $Co_{0.25}Ni_{0.25}Zn_{0.25}Cu_{0.25}Fe_2O_4$ NSFs.

2 Experimental

2.1 Chemicals and Instrumentations

The following chemicals have been received from Merck ($Cu(NO_3)_2.3H_2O$ (99.9%), $Ni(NO_3)_2.6H_2O$ (≤ 98.5%), $AgNO_3$ (≤ 98.5%), $Zn(NO_3)_2.4H_2O$ (≤ 98.5%), $Co(NO_3)_2.6H_2O$ (≤ 98.5%), and $Fe(NO_3)_3.9H_2O$ (≤ 98%) and urea (NH_2CONH_2) (≤ 98%) and used without further purification. Structural investigation of produced composites was examined via an X-ray diffractometer (XRD; Rigaku MiniFlex 600) with Cu$K\alpha$ radiation (**λ = 1.5406 Å**). The XRD measurements were taken with 2θ angle range of from 20 to 80° with a step of 0.02°. The obtained patterns were analyzed with the help of Match 3 software to identify precisely the different phases. The morphology was investigated using scanning electron microscopy (Tescan VEGA SEM) and high-resolution transmission electron microscopy (HR-TEM, Thermo Talos) with an acceleration voltage of 10 kV, a spot size of 3.0, and a working distance of 9.7 mm. The elemental compositions and their atomic percentage were assessed using an EDX spectroscopy attached to the SEM. A Novocontrol Alpha impedance analyzer was used for conductivity and dielectric measurements. The proton conductivity studies, and dielectric measurements of the NSFs were performed using a Novocontrol impedance spectrometer. The films were sandwiched between gold blocking electrodes, and the conductivities were measured in the frequency range 0.1 Hz–3 MHz at 10 °C intervals between 20 and 120 °C.

2.2 Synthesis

The Ag → CoNiZnCu ($x \leq 0.10$) NSFs were fabricated via the one-pot sol–gel method for which urea was used as fuel. The synthesis method was proceeded by dissolving the stoichiometric amount of metal nitrates and 8 g urea in 30 ml of deionized H_2O (DI water) together under a constant stirring at 80 °C for 30 min to get a homogeneous mixture. Then, the pH of the resultant mixture of 7 was attained by the addition of ammonia solution where the temperature increased from 110 to **330** °C and constantly stirred until the gel formed. Through the heating procedure, the resultant gel was burnt to get black powder (self-propagating combustion). The obtained solid product did not have any calcination process (Scheme 1) [30].

3 Results and Discussion

3.1 Structure and Morphology

XRD powder patterns of Ag → CoNiZnCu ($x \leq 0.10$) NSFs are given in Fig. 1. The observed diffraction peaks closely match those of a mixed spinel ferrite nanocomposite, confirming its phase purity. Notably, Ag^+ ion substitution did not alter the cubic spinel structure of the nanocomposite; however, it caused slight broadening of the most intense peak at the (311) plane. This peak broadening indicates a reduction in crystal size with increasing Ag ion substitution. Structural parameters such as lattice constant a (Å), cell volume V ($Å^3$), XRD density dx (g/cm^3), and hopping lengths at Site-A (L(A)) and Site-B (L(B)) of the mixed spinel ferrite nanocomposite were calculated and are summarized in Table 1. Crystal size was determined using the Scherrer equation at the (311) peak, along with the Williamson–Hall (W–H) method. The lattice constant initially increased and then decreased in the substituting range of $x = 0.06-0.10$, which is attributed to the mismatch in ionic radii between Ag and Fe ions. The crystallite sizes were found to range between 19 and 40 nm according to the W–H analysis. Furthermore, W–H analysis

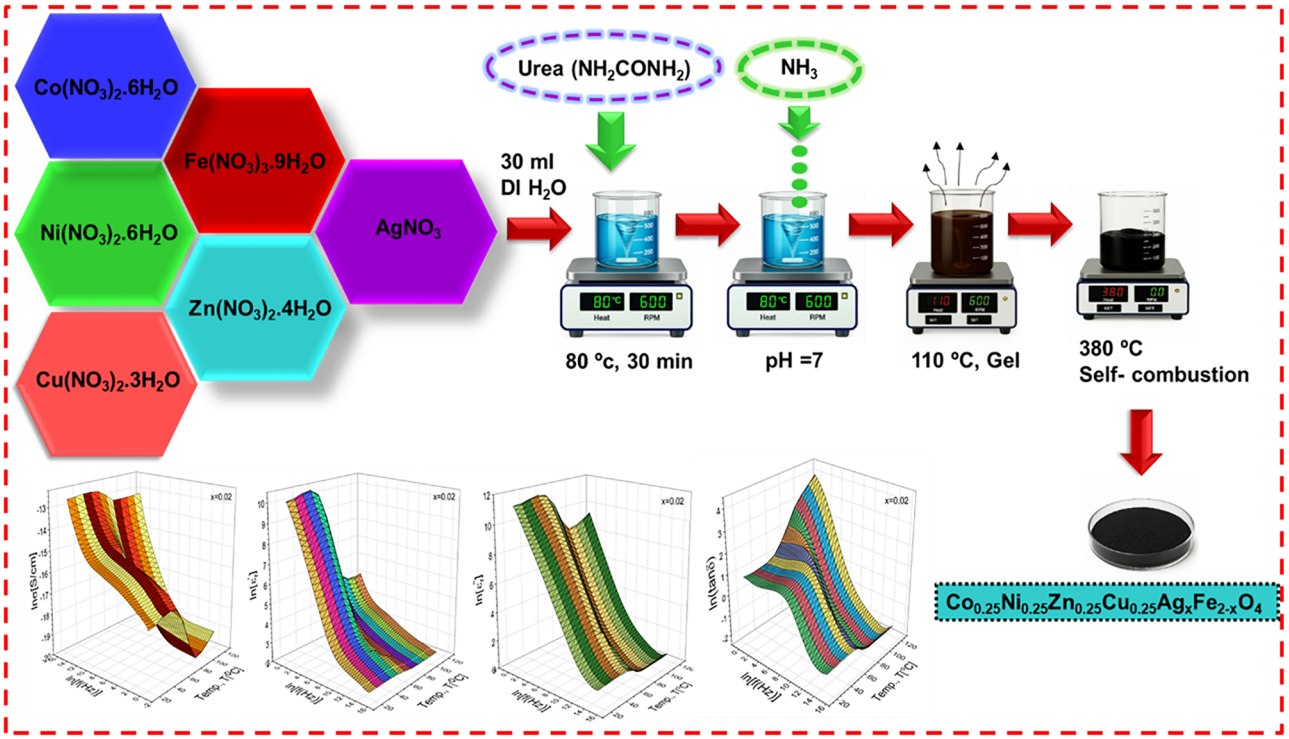

Scheme 1 One-pot sol–gel synthesis of Ag → CoNiZnCu (x ≤ 0.10) NSFs

Table 1 Structural parameters of Ag → CoNiZnCu (x ≤ 0.10) NSFs

X	a (Å)	MW (g/mol)	dx (g/cm^3)	V (Å)^3	Dp (Scherrer) (nm)	Dp (W–H) (nm)	Micro-strain (ε) W–H × 10^{-4}	L(A) (nm)	L(B) (nm)	R_{Bragg}	χ2
0.00	8.351	237.775	5.355	582.340	30.88	27.16	7.1	3.616	2.952	17.8	1.15
0.02	8.354	238.816	5.345	582.949	21.31	19.04	4.5	3.617	2.953	29.1	1.57
0.04	8.371	239.856	5.357	586.630	26.16	21.29	8.25	3.625	2.960	33.3	1.48
0.06	8.357	240.897	5.318	583.560	28.82	24.86	19.2	3.619	2.954	23.5	1.17
0.08	8.351	241.937	5.360	582.340	43.69	37.81	27.7	3.616	2.952	31.5	1.23
0.10	8.339	242.978	5.350	579.911	36.29	38.68	34.9	3.611	2.948	20.4	1.13

revealed that a positive slope corresponds to tensile strain (Fig. 2) [31].

Scanning electron microscopy (SEM) was used to examine the morphology of Ag → CoNiZnCu (x ≤ 0.10) NSFs nanostructured ferrites (NSFs), as shown in Fig. 3. The SEM images reveal agglomerated, spherical-shaped particles. Due to substitution, a more nonuniform particle morphology was observed. The chemical composition of (Ag → CoNiZnCu (x = 0.02 and 0.06)) NSFs was quantitatively confirmed using energy-dispersive X-ray spectroscopy (EDX), as presented in Fig. 4. The EDX spectra show the weight percentages (wt.%) of the elements Co, Ni, Zn, Cu, Ag, Fe, and O. Further analysis of particle shape and phase formation for Ag → CoNiZnCu (x = 0.02) NSFs was carried out using TEM and HR-TEM, as illustrated in Fig. 5. TEM images indicate a tendency toward spherical nanoparticle formation, while HR-TEM confirmed the spinel ferrite structure, consistent XRD observations.

3.1.1 Cation Distribution

The cation distribution of the synthesized spinel ferrite system Ag → CoNiZnCu (x ≤ 0.10) NSFs was systematically determined using the modified Bertaut refinement method applied to X-ray diffraction (XRD) data. The method is based on minimizing the R_{obs} value derived from the absolute differences between experimental and calculated intensities of selected cation-sensitive diffraction planes: (220), (400), (422), and (440) [32].

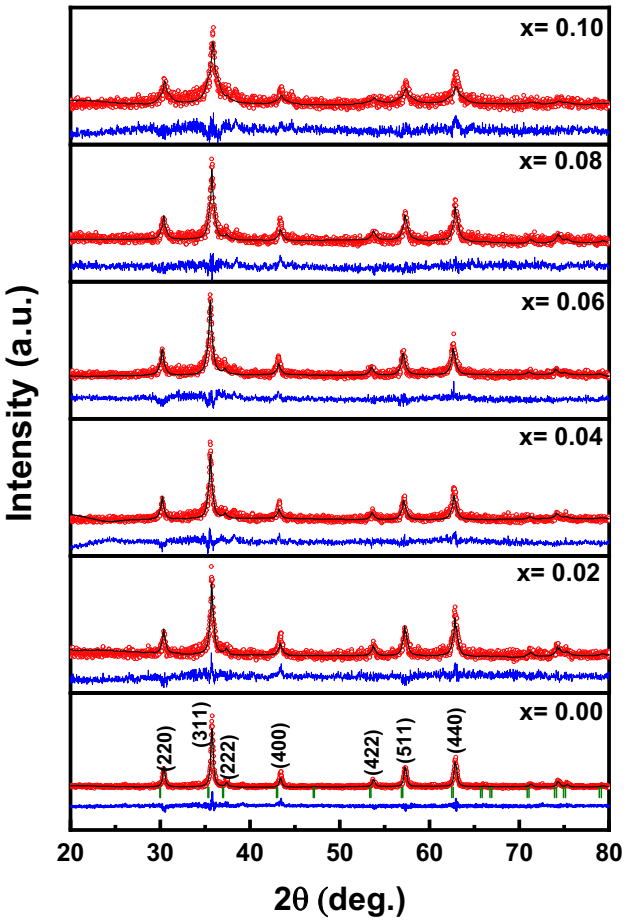

Fig. 1 XRD powder patterns of Ag → CoNiZnCu (x ≤ 0.10)) NSFs)

The theoretical intensity of each selected Bragg reflection is calculated by evaluating the structure factor, which accounts for the atomic form factors of individual ions and their respective occupancies at tetrahedral (T_d, A) and octahedral (O_h, B) sites. This calculation also includes corrections for multiplicity and Lorentz-polarization effects to ensure accuracy. R_{obs} is a parameter that quantifies how closely experimental results agree with theoretical predictions; it is the sum of the absolute differences between experimentally observed intensity ratios and those predicted by theory. Minimizing R_{obs} is important; a R_{obs} value approaching zero indicates a distribution of cation species that closely matches the experimental diffraction pattern. Robs is minimized using an evolutionary algorithm with two constraints: to conserve charge neutrality and to have a fixed total occupancy of the sites.

All optimization cycles are completed with respect to the following conditions: the predetermined upper and lower bounds of occupancy for cations, that at A- and B-site the total cation content is equal to the expected stoichiometric amount, and the overall electrostatic balance; thus, a significant difference from one would be interpreted as being due to the presence of an oxygen vacancy, which is the typical mode of compensation for non-stoichiometric spinel's [33, 34].

The refined cation distribution suggests that the A-site population remains nearly unchanged with x. Within this model, Ag^+ incorporation is inferred to influence the B-site environment more strongly than the A-site environment.

As more Ag^+ ion is added to the structure, there will be an increase in the number of Ag^+ ions substituted on the B-site at an increasing rate; as well, the fact that Ag^+ ion has a larger ionic radius (˜1.15 Å) and has less preference for Td coordination compared with other cations that could fit in the B-site position suggests that the addition of Ag^+ ion will result in a steady decline in the amount of Fe^{3+} in both sites when the total amount of Ag^+ ion is increased from 0.02 to 0.10, which indicates to replace or to redistribute Fe^{3+} between both sites in order to maintain the charge balance of the system.

i. The levels of Ni^{2+} and Co^{2+} stay almost equal ($Ni_{0.02}$ and $Co_{0.02}$) and thus support the fact that they are both in two different sites, but there is a greater preference for them being in the Oh site.

ii. Cu^{2+} is generally considered to favor octahedral coordination because of Jahn–Teller stabilization; thus, the refinement trend is consistent with limited redistribution of Cu^{2+} under Ag^+ substitution, although this is not directly proven here.

This means that the different cations have different locations that would be consistent with their energy and size; therefore, they can all be readily replaced and compensated for by other cation species that can be used to accommodate the overall charge balance in the material. Since we know that when one cation replaces another cation with a lower charge and that the structure is electrically neutral, in the case of replacing monovalent Ag^+ for trivalent Fe^{3+} this will create a net deficit of positive charge in the structure. For example, substituting one Ag^+ for one Fe^{3+} reduces the positive charge by 2 units for each substitution of Ag^+ for Fe^{3+}. In order to maintain an electrically neutral structure, the system has to compensate for this deficit, i.e., (1) Fe^{3+} will be redistributed to the A-site of the spinel. This can be seen indirectly from the small decrease in Fe content on the A-site; (2) oxygen vacancies will be created as another mode of compensatory mechanism in spinel ferrites.

The decrease in the refined B-site Fe^{3+} content together with the increasing Ag^+ contribution is consistent with possible defect formation and/or charge-compensation processes, although direct spectroscopic verification would be required for confirmation.

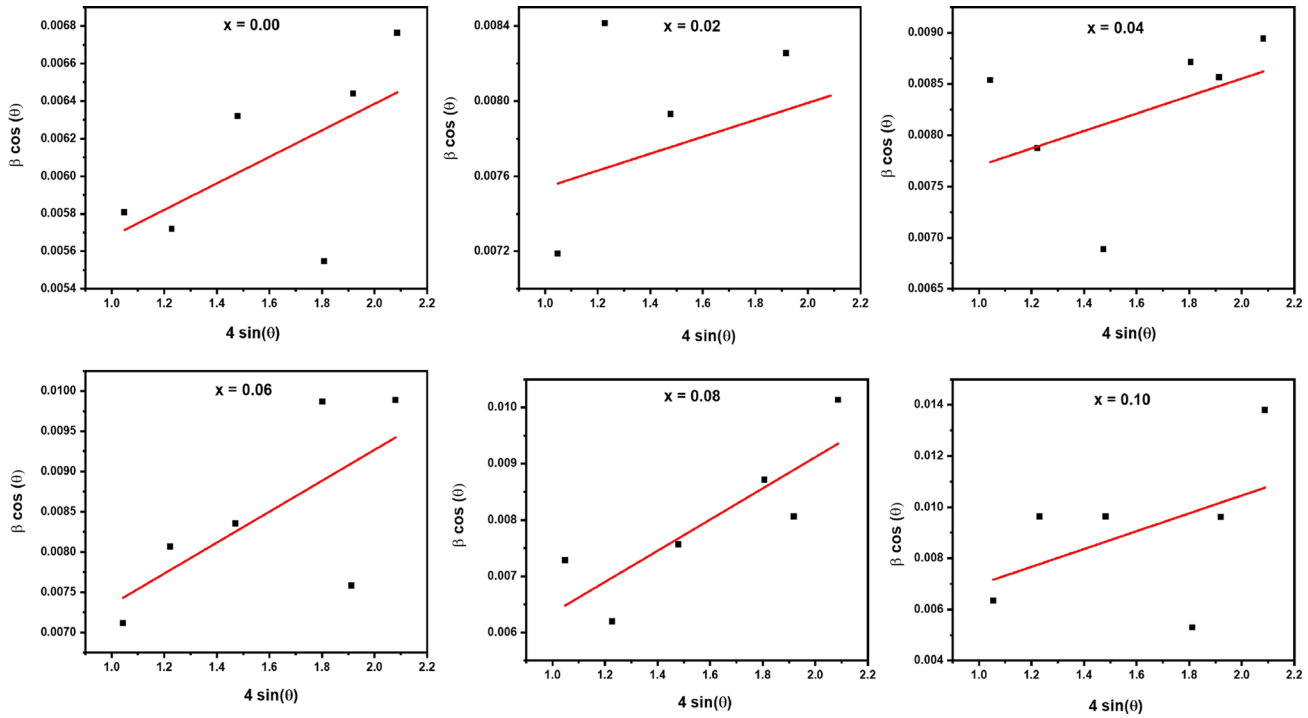

Fig. 2 Williamson–Hall plots of Ag → CoNiZnCu (x ≤ 0.10)) NSFs

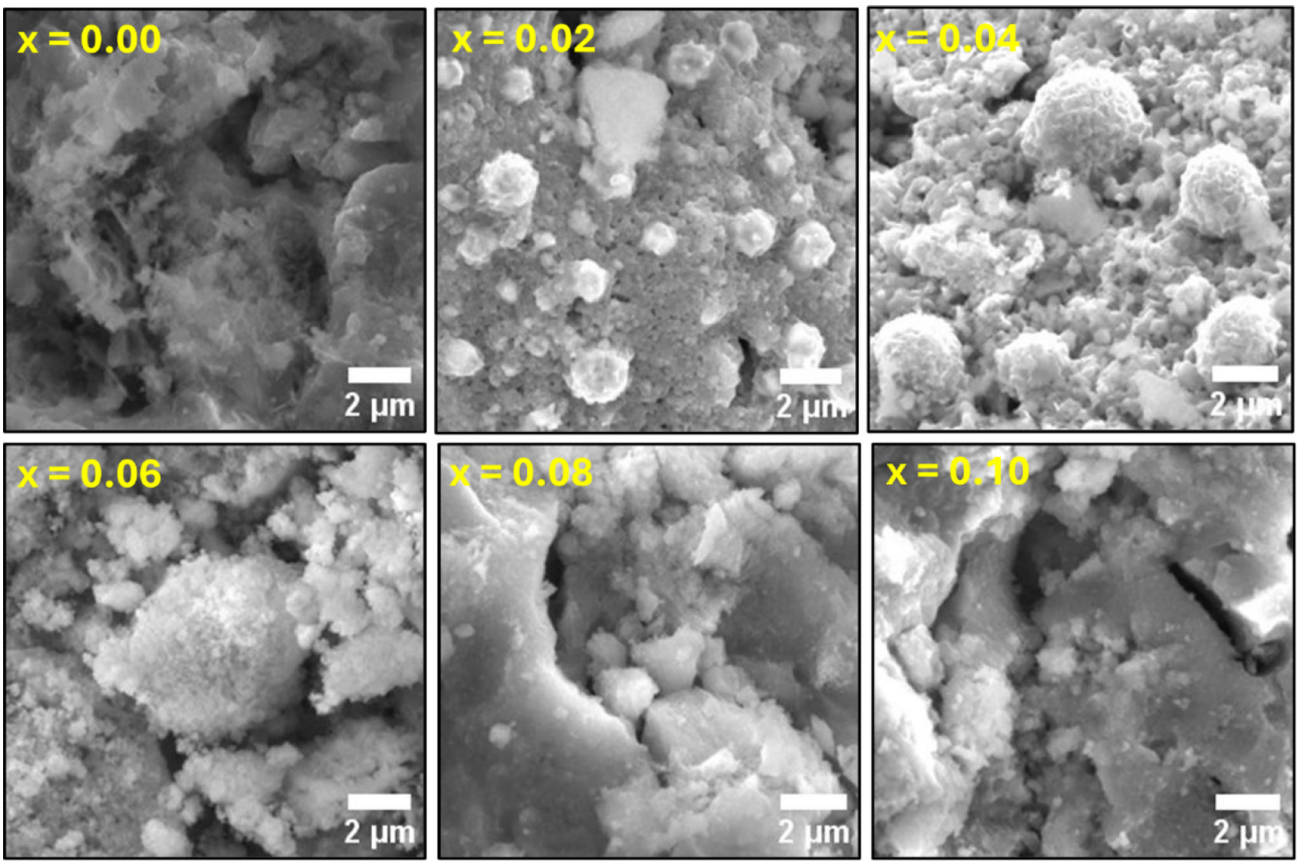

Fig. 3 SEM micrographs of Ag → CoNiZnCu (x ≤ 0.10)) NSFs

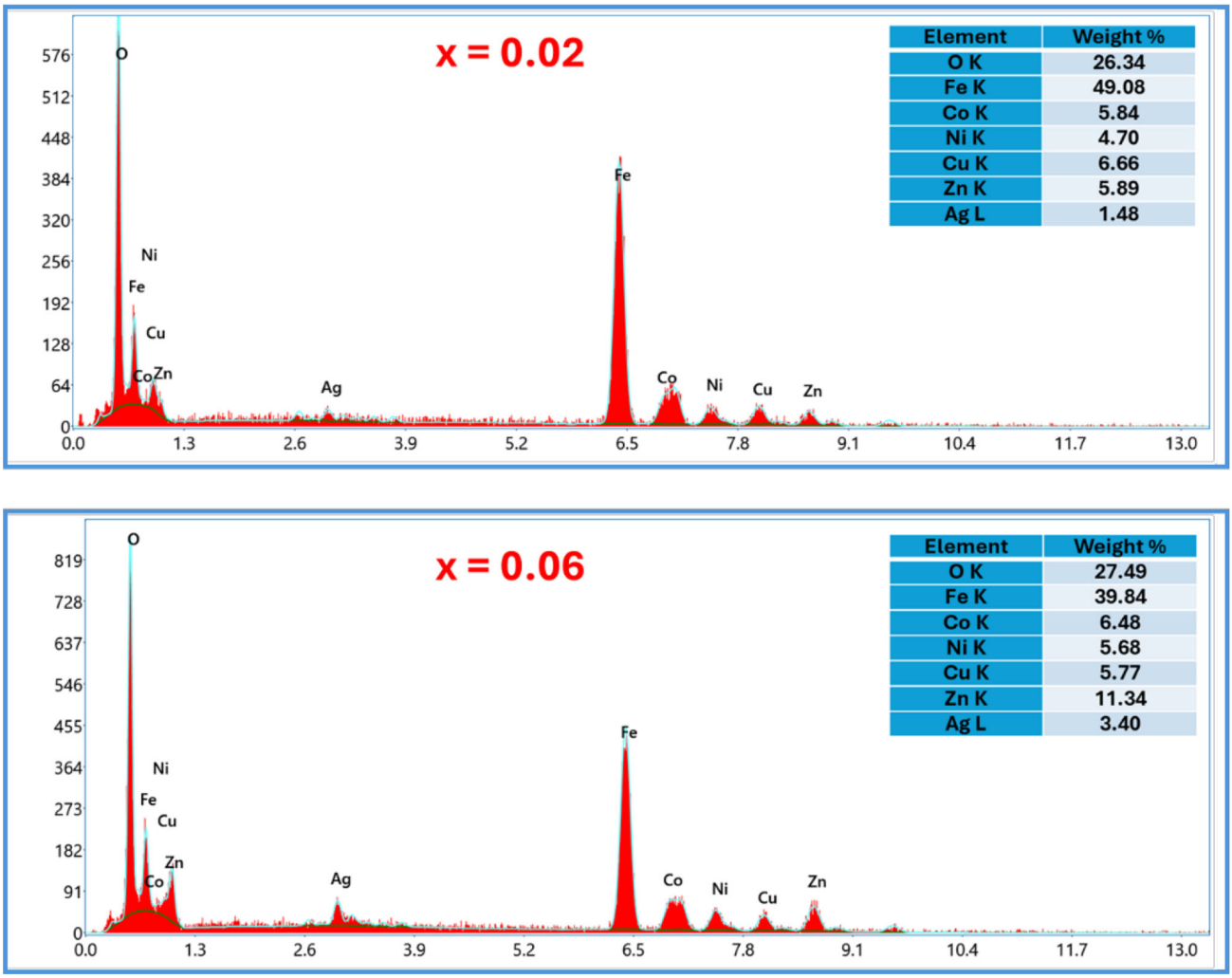

Fig. 4 EDX spectra of Ag → CoNiZnCu (x = 0.02 & 0.06) NSFs

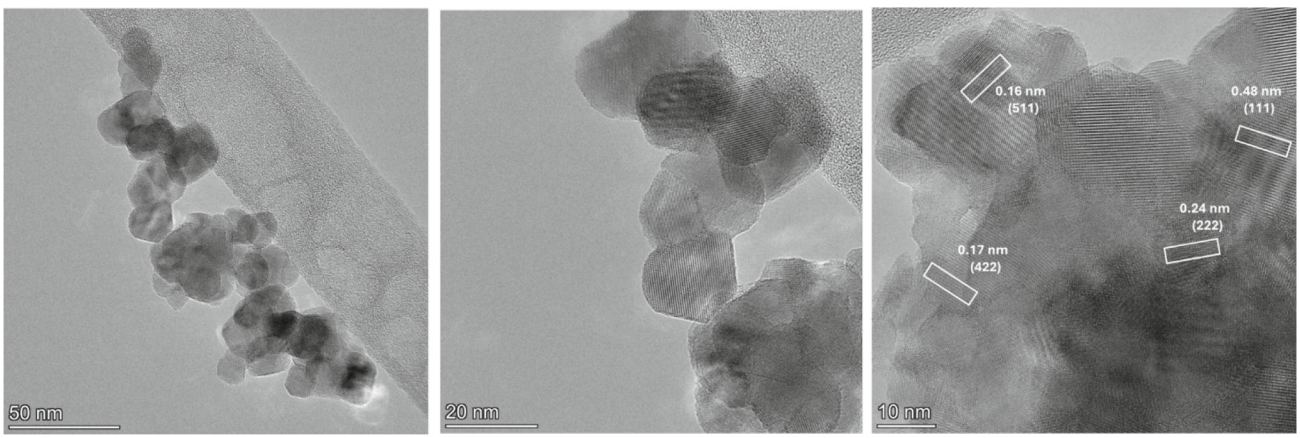

Fig. 5 TEM and HR-TEM images of Ag → CoNiZnCu (x = 0.02) NSFs

3.1.2 Agglomeration-Driven Electrical Heterogeneity

As clearly seen in the SEM micrographs, although it reveals pronounced particle agglomeration, this situation may be consistent with electrical modeling based on grain and grain boundary contributions. In NSF systems synthesized by sol–gel methods, agglomeration typically leads to the formation of electrically connected grain clusters; thus, each cluster can behave like a network of nanoscale grains separated by internal interfaces. Therefore, the concept of "grains" in impedance analysis is more reasonably interpreted as electrically active regions within clustered groups rather than isolated, geometrically distinct particles [35].

From an electrical perspective, these agglomerated structures likely increase the complexity of the grain boundary network, leading to a distribution of interface barriers with varying thicknesses and conductivities. This appears consistent with the observed non-Debye relaxation behavior modeled using a constant phase element (CPE) in the EEC. As explained in later sections, the depressed semicircles in the Nyquist plots and the broad relaxation peaks in the dielectric loss and modulus spectra further confirm the existence of distributed relaxation times arising from structural heterogeneity caused by agglomeration [36].

Furthermore, agglomeration can significantly affect the MW interface polarization. Interconnected grain clusters create extended channels for charge transport within the grains, while also increasing the formation of internal interfaces where charge carriers accumulate. Thus, this type of formation contributes to increased space charge polarization at low frequencies and the observed enormous dielectric constant. However, excessive agglomeration also makes it possible for conductive channels to leak along grain boundaries, effectively reducing barrier resistance and leading to "leaky capacitor" behavior at higher substitution levels, as observed in the decrease in dielectric constant beyond $x \approx 0.02$.

Therefore, the coexistence of different grain/grain boundary electrical responses and agglomerated morphology is physically consistent. Both impedance and modulus analyses rely on regions that cannot be formed by perfectly isolated grains, but rather on electrically discernible, highly agglomerated NSFs, which remain valid even in these compositions. This elucidation is consistent with the evolution of grain boundary resistance, relaxation peaks, and dielectric dispersion behavior observed across all NSFs 37, 38].

3.2 Electrical Properties: Conductivity Analysis

3.2.1 *AC Conductivity (σ_{AC})*

The thermal activation process generally occurs in all NSFs through electrical current conduction. Electrical conduction in conductors is a specific case of behavior observed in thermally active semiconductors, where the AC conductivity (σ_{AC}) increases significantly with rising temperature. It can be known that the primary mechanism behind conduction mechanisms in these NSFs becomes the mobility of charge carriers, mainly electrons, which hop or transfer between ferrous (Fe^{2+}) and ferric (Fe^{3+}) ions located at the O_h (or B) site of the spinel structure. Consequently, charge carrier-assisted conduction in these thermally active mechanisms follows an Arrhenius-type relation where $\sigma_{AC} = \sigma_0 e(-E_A/k_B T)$, indicating that higher thermal energy enhances charge carrier mobility and their exchange [37].

Most of the substituted NSFs exhibit frequency dependence in their σ_{AC}, as described by the $\sigma_{DC} + A\omega^s$ equation from well-known Jonscher's Universal Power Law. The Maxwell–Wagner (MW) model provides a logical explanation for this behavior [38]. According to this model, some NSF consists of highly conductive grains separated by less conductive grain boundaries. At lower frequencies, charges must cross the resistive grain boundaries, leading to long-range hopping process between grains and a stable conductivity level at σ_{DC} regime. When frequencies become higher, the capacitive effect across grain boundaries effectively bypasses their resistive one, allowing charges to hop only short distances within individual intra-grains. This causes a sharp increase in **conductivity**, known as strong dispersion (Table 2).

The principles embodied in these concepts are illustrated in Fig. 6. So, six separate 3D surface plots display the AC conductivity of Ag-to-Co–Ni-Zn-Cu NSFs ($x \leq 0.10$) as a function of both frequency and temperature. Each plot depicts an NSF with an Ag substitution ratio, 'x', ranging from 0.00 to 0.10. The three dimensions of each plot correspond to the AC conductivity of each NSF, $\ln\sigma_{AC}$, ln(f) (frequency), and T (temperature). Validated predictions about the behavior of AC conductivity across all substitution levels are shown through the datasets of the various plots,

Table 2 Cation distribution of Ag → CoNiZnCu ($x \leq 0.10$) NSFs

x	T_d (A-site)	O_h (B-site)
0.00	$Co_{0.05}Zn_{0.25}Ni_{0.05}Fe_{0.65}$	$Co_{0.20}Cu_{0.25}Ni_{0.20}Fe_{1.35}$
0.02	$Zn_{0.25}Ni_{0.05}Co_{0.05}Fe_{0.65}$	$Co_{0.2}Ni_{0.2}Cu_{0.25}Ag_{0.02}Fe_{1.33}$
0.04	$Zn_{0.25}Ni_{0.05}Co_{0.05}Fe_{0.65}$	$Co_{0.2}Ni_{0.2}Cu_{0.25}Ag_{0.04}Fe_{1.31}$
0.06	$Zn_{0.25}Ni_{0.05}Co_{0.05}Fe_{0.65}$	$Co_{0.2}Ni_{0.2}Cu_{0.25}Ag_{0.06}Fe_{1.29}$
0.08	$Zn_{0.25}Ni_{0.05}Co_{0.05}Fe_{0.65}$	$Co_{0.2}Ni_{0.2}Cu_{0.25}Ag_{0.08}Fe_{1.27}$
0.10	$Zn_{0.25}Ni_{0.05}Co_{0.05}Fe_{0.65}$	$Co_{0.2}Ni_{0.2}Cu_{0.25}Ag_{0.10}Fe_{1.25}$

Site occupancies are inferred from modified Bertaut refinement of XRD intensity ratios and should not be interpreted as direct spectroscopic confirmation of cation positions

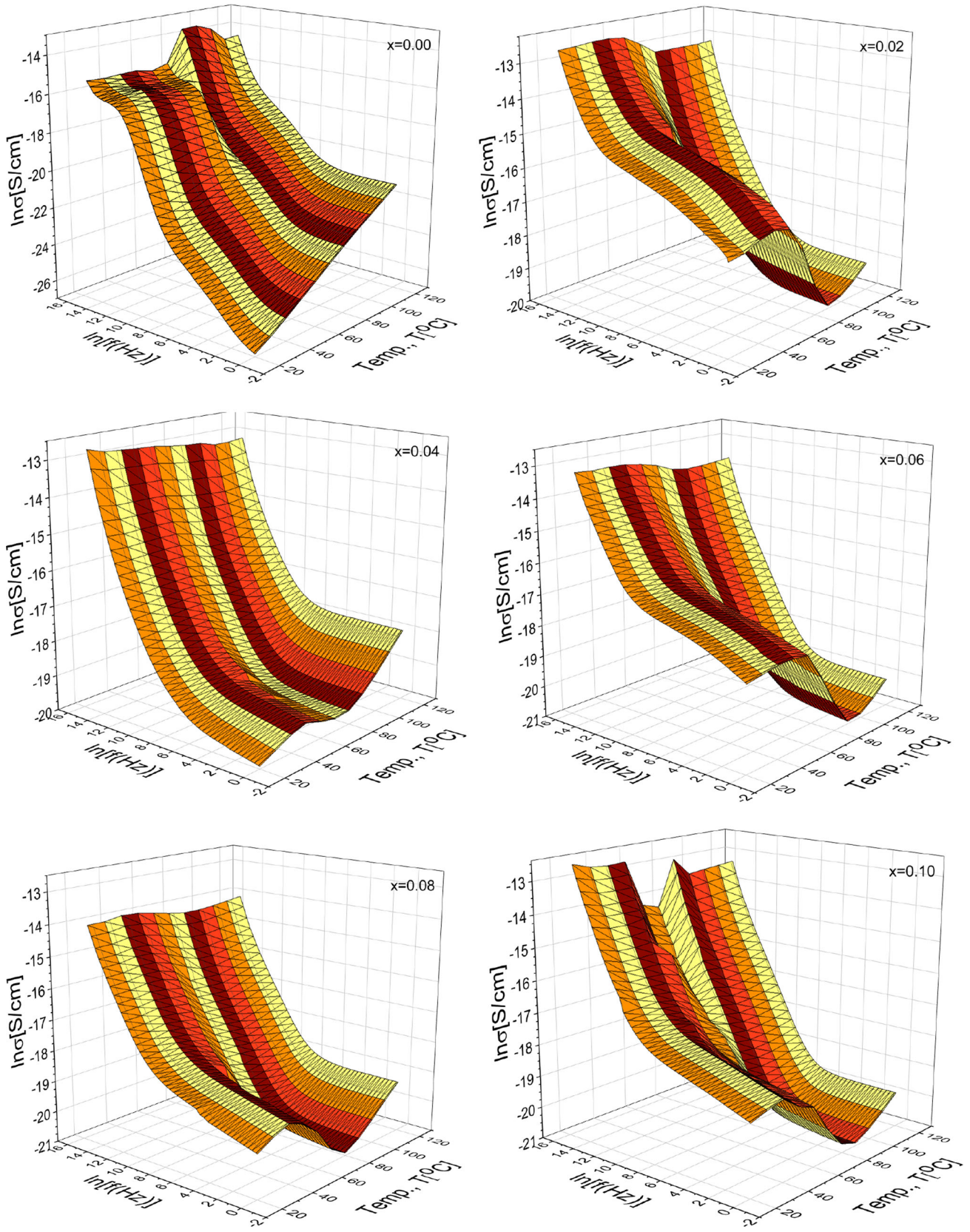

Fig. 6 3D illustration of the AC conductivity of Ag → CoNiZnCu (x ≤ 0.10) NSFs

where increasing temperature and frequency consistently enhance AC conductivity at all levels of Ag substitution.

Graphs show that substituting Ag^+ ions for Fe^{3+} ions has been a main focus of the study. Comparing the graphs, there is a general trend of decreasing σ_{AC} as the substitution ratio, 'x', for the Ag ions increases from x = 0.00 to x = 0.10. As mentioned, the primary mechanism by which charges move is hopping between Fe^{2+} and Fe^{3+} ions. Using monovalent Ag^+ ions, which do not participate in charge transport, to replace Fe^{3+} ions reduces the number of active hopping sites for charge movement between Fe ions. Because the number of conduction sites has been reduced, macroscopic conductivity will decline.

Along with the main trend previously described the effect of sublimating the primary metal will likely influence the new material's behavior through its microstructure. An example of this is the 'hump' or distortion observed at both lower frequencies and elevated temperatures for x = 0.00 and 0.10, which is associated with grain-boundary and/or electrode-polarization phenomena. The variation in the characteristics of this hump based on 'x' suggests that substituting Ag^+ ion into the NSFs will alter the electrical properties of the grain boundaries, possibly through increased segregation and thus affect the MW relaxation phenomena.

Furthermore, the 3D graphics provide a clear visual representation of how temperature, frequency, and Ag ion substitution interact, as well as how these interactions affect the electrical transport mechanism of the complex NSF system, designated by $\sigma_{AC}(\omega)$. The data also confirm that the processes influencing $\sigma_{AC}(\omega)$ are thermally activated, involve electron hopping, and are affected by MW interfacial polarization at grain boundaries, as predicted by established theory [20]**.** A significant observation when systematically substituting Ag^+ ions with Fe ions is seen to be a decrease in conductivity, which is related to the reduced number of available (ferrous-ferric) ion pairs ($Fe^{2+} - Fe^{3+}$) that facilitate charge conduction through the grains.

3.2.2 Transport Mechanisms (JPL modeling)

The conductivity's frequency response in all Ag → CoNiZnCu NSFs adheres to Jonscher's universal power law, $\sigma(\omega) = \sigma_{DC} + A\omega^s$, as shown by the linear $\ln(\sigma_{AC})$–$\ln(f)$ trend in the high-frequency dispersive region (Fig. 7). The frequency exponent s, derived from the slopes of these linear regions, is listed in Table 3 for different temperatures and Ag substitutions. As indicated, *s* ranges from 0.75 to 0.84 at 20 °C and decreases gradually with increasing temperature, reaching 0.60 to 0.70 at 120 °C across all compositions. A slight but consistent decline in *s* with rising Ag ion substitution ratio at a constant temperature suggests a gradual delocalization of carriers and a reduction in effective hopping barriers within the grains. The observed decrease of *s* with temperature is characteristic of the correlated barrier hopping (CBH) model, unlike other mechanisms such as non-overlapping small polaron tunneling (NSPT) or overlapping large polaron tunneling (OLPT), which do not match the trends in Table 3. It is also evident to highlight that the CBH model explains the differences between σ_{DC} and σ_{AC} of the high frequency. Moreover, the low-frequency conductivity plateau, σ_{DC}, arises from long-range charge transport across high-resistance grain boundaries, with lower magnitude and higher thermal activation. Conversely, σ_{AC} of the dispersive high frequency arises mainly from localized hopping within the grains, where charge carriers respond to the applied field without crossing grain boundaries.

Consequently, σ_{AC} grows more quickly with elevating both frequency and temperature than σ_{DC}, suggesting a shift from grain-boundary-limited DC conduction to grain-controlled AC conduction. This behavior complements the conductivity analysis, the *s* values listed in Table 3, and the contributions from grains and grain boundaries derived from impedance measurements. Thus, the observed decrease in '*s*' with increasing temperature is characteristic of the CBH model, indicating that thermally activated hopping between localized states is the primary mechanism for AC conduction. To clarify, this distinction can be summarized as follows:

Transport regime	*Frequency range*	*Dominant microstructural element*	*Physical mechanism*
σ_{DC} plateau	Low frequency	Grain boundaries	Barrier-limited hopping
σ_{AC} dispersion	High frequency	Grains	Localized CBH hopping

Therefore, this complementary interpretation improves the internal consistency among conductivity, impedance, and dielectric analyses presented.

3.2.3 *DC Conductivity (σ_{DC}) and Activation Energy (EA)*

The temperature effect on the DC electrical conductivity of semiconducting non-stoichiometric ferrites increases or decreases, respectively, according to the Arrhenius equation: $\sigma_{DC} = \sigma_0 \exp(-E_A/k_BT)$, where σ_0 is the pre-exponential factor or intercept on the y-axis in the logarithmic plot of σ_{DC}; E_A is the activation energy (the energy needed to move charge between neighboring ions); k_B is Boltzmann's constant; and T is the absolute temperature measured in Kelvin. E_A can be determined directly from the slope of the linear sections of the Arrhenius plot of σ_{DC} versus $(1/k_BT)$.

The Arrhenius plots of the Ag → CoNiZnCu (x ≤ 0.10) NSFs are shown in Fig. 8. There are two main similarities

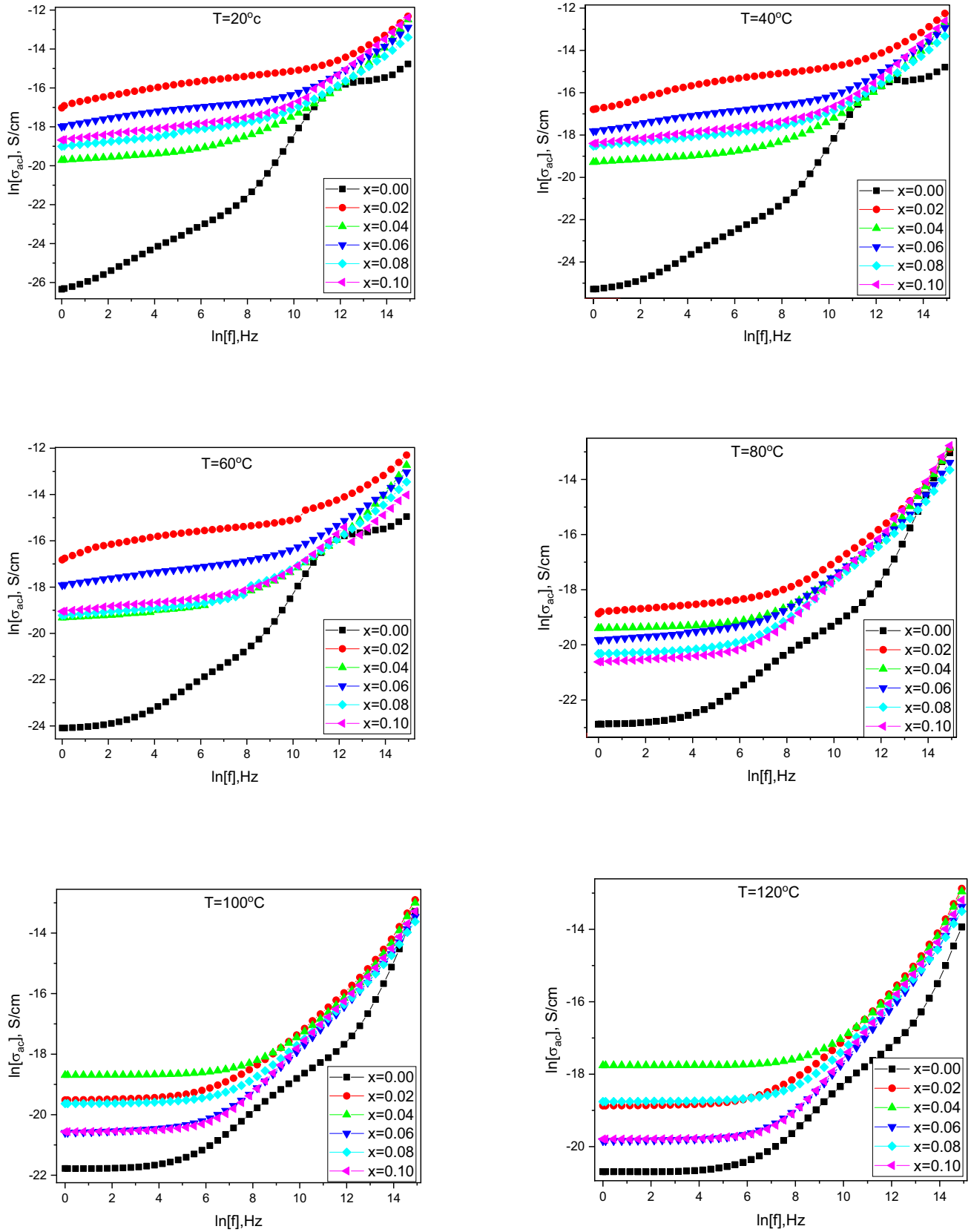

Fig. 7 AC conductivity of Ag → CoNiZnCu (x ≤ 0.10) NSFs for different levels of Ag substitution

Table 3 Approximate frequency exponent (s) derived from $\ln(\sigma_{AC})$ versus $\ln(f)$ plots for Ag → CoNiZnCu NSFs

x/Temp. (°C)	0.00	0.02	0.04	0.06	0.08	0.10
20	0.84	0.82	0.80	0.78	0.76	0.75
40	0.82	0.80	0.78	0.76	0.74	0.72
60	0.79	0.77	0.75	0.73	0.71	0.69
80	0.76	0.74	0.72	0.70	0.68	0.66
100	0.73	0.71	0.69	0.67	0.65	0.63
120	0.70	0.68	0.66	0.64	0.62	0.60

Note that the frequency exponent s was derived from the slope of the linear high-frequency region of $\ln(\sigma_{AC})$ versus $\ln(f)$ plots, which follow Jonscher's power law

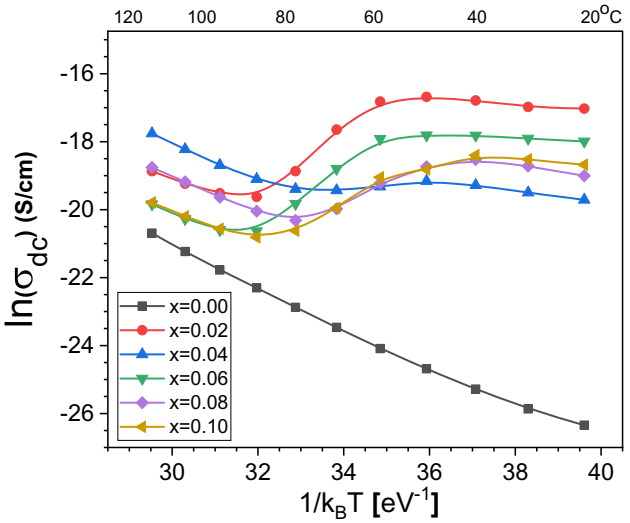

Fig. 8 Arrhenius plot of the DC conductivity for Ag → CoNiZnCu (x ≤ 0.10) NSFs

observed in all these materials. The first is that the conductivity increases with temperature (meaning $\ln\sigma_{DC}$ becomes less negative as $1/k_BT$ decreases); this indicates that the NSFs are semiconductors, confirming that they follow a thermally activated electron-hopping mechanism [39]. A second similarity is that the plots are not perfectly straight lines over the tested temperature range. Most of the NSFs show a clear change in slope (known as "knee"), indicating a change in the value of EA [40].

One of the most interesting features of the graph is the very large effect of substituting Ag ions on the DC conductivity of NSFs. The unsubstituted NSF (x = 0.00) has very low σ_{DC}, with the lowest value being several orders of magnitude lower than that with Ag substitution. Once a small amount of Ag ions is introduced to the NSF (i.e., for x = 0.02), σ_{DC} increases dramatically across all other Ag substitutions (i.e., for x > 0.02). Additionally, the DC conductivities for each substituted NSF remain significantly higher than that of the unsubstituted NSF, although there is a non-monotonic trend among the substituted NSFs, with the peak occurring at x = 0.02.

The situation may seem contradictory when examined in light of the results from high-frequency σ_{AC} tests (as shown in Fig. 6), which show a general decrease in σ_{AC} with Ag ion substitution. However, the discrepancy between these two data sets can be explained by considering that the NSF microstructure is polycrystalline (as described by the MW model [18, 28]) and can therefore be viewed as an inhomogeneous material made up of individual grains (with high conductivities) interconnected through less conductive grain boundary networks (high resistance). In terms of σ_{DC} measuring stopping power, this grain boundary network, being the most resistive part of the current path, acts as a limiting factor; thus, for σ_{DC}, the current must always pass through the grain boundaries (the limit) before reaching the next conductive grain, ensuring that the resistive element is always part of the current path. Conversely, for σ_{AC} measurements of stopping power, the high frequency of testing mostly affects σ_{AC} by the local motion of charge carriers (electrons, holes, etc.) within each conductive grain, which promotes favorable behavior and allows charge carriers to bypass the resistive grain boundaries.

The evidence from both AC and DC measurements strongly indicates that Ag ions serve two functions. The first function, substitution, was demonstrated by substituting some Fe ions (Fe^{2+} with Fe^{3+}), which caused slight disruptions in the chain-like structure of the Fe^{2+}—Fe^{3+} (hopping chains), thereby reducing the intrinsic conductivity for each grain, as shown by the high-frequency data trends in AC measurements. The second function is that most Ag ions tend to migrate to grain boundaries, where they are segregated by segregation boundaries, thus lowering the resistivity of these NSFs. Therefore, the increase in σ_{DC} caused by substituting Ag ions is mainly due to enhanced conductivity arising from the segregation of Ag ions at grain boundaries, which explains the significant increase in σ_{DC} observed compared to the base NSF.

Table 4 Activation energies (E_A's) for three regions obtained from DC Arrhenius plots

Ag content (x)	(E_{A1}) eV (Region-I)	(E_{A2}) eV (Region-II)	(E_{A3}) eV (Region-III)
0.00	0.31	0.47	0.62
0.02	0.18	0.36	0.51
0.04	0.14	0.29	0.44
0.06	0.20	0.43	0.57
0.08	0.11	0.25	0.39
0.10	0.16	0.32	0.48

An Arrhenius analysis of Ag ion substitution reveals a thermally activated, semiconducting behavior in these Ag-substituted NSFs, with a noticeable change in E_A at the Curie temperature. The most significant instinct arises from the reliable results of both AC and DC measurements, which suggest that Ag primarily enhances electrical conduction mechanism by improving grain boundary conduction. This positive impression on grain-boundary conductivity surpasses the reduction within the grains, highlighting the importance of microstructural engineering in adjusting the electrical properties of NSFs.

Figure 8 presents the Arrhenius plots of the DC conductivity for Ag → CoNiZnCu (x ≤ 0.10) NSFs over the entire temperature range studied. Thus, all the NSFs depict clear deviations from single-slope Arrhenius behavior, suggesting the presence of multiple thermally activated conduction mechanisms. As a result, the temperature dependence of σ_{DC} can be categorized into three regions: high-temperature (Region-I), intermediate-temperature (Region-II), and low-temperature (Region-III). The activation energies derived from linear fits in each region are listed in Table 4.

In Region-I (high-temperature range), low activation energies (0.11–0.31 eV) are observed, indicating thermally assisted short-range charge hopping within grains. The lower energy barriers indicate improved carrier mobility, especially in Ag ion-substituted NSFs, where substituting Ag ions supports charge compensation and enhances the number of mixed-valence Fe^{2+}/Fe^{3+} pairs.

In the intermediate-temperature range (Region-II), higher activation energies (0.25–0.47 eV) are perceived, reflecting the combined conduction effects of both grain and grain-boundary. This aligns with the MW interfacial polarization model, which suggests charge buildup at grain boundaries causes a formation of additional potential barriers.

In the lower-temperature range (Region-III), the highest activation energies, between 0.39 and 0.62 eV, are observed, indicating that charge carriers are highly localized and transport contribution is mainly dominated by grain boundaries. The rising activation energy in this region suggests that carrier mobility relies on defect-assisted hopping and encounters potential barriers arising from structural disorder and intergranular interfaces. Importantly, substituting with Ag ions reduces activation energies across all three regions, confirming their role in lowering hopping charge barriers and enhancing electrical conduction. These results show that the DC conduction mechanism in Ag-substituted NSFs shifts with temperature: from grain-controlled hopping at higher temperatures to grain-boundary-limited transport at lower temperatures.

3.3 Complex Dielectric Analysis

3.3.1 *Dielectric Constant (ϵ_r')*

The dielectric properties of NSFs are determined by the polarization mechanisms, including electron, ionic, dipole, and interfacial (space-charge) polarization. Each of these mechanisms responds differently to an external electric field, depending on the field's frequency. At high frequencies, only the fast-acting electronic and ionic polarizations contribute to the response, resulting in a lower dielectric constant (ϵ_r') for the NSF. As the frequency decreases, the slower polarization mechanisms have enough time to become active, leading to a significant increase in the value of ϵ_r' for NSFs due to dielectric dispersion.

In NSFs, the dominant low-frequency mechanism is MW interfacial polarization [37, 38]. This model describes NSF as composed of highly conductive grains separated by thin, more resistive boundaries that respond in a specific way. When a field is applied, charge carriers—electrons hopping between Fe^{2+} and Fe^{3+}—move freely within the grains but are blocked at the grain boundaries, leading to accumulation. This space charge accumulation produces many macroscopic dipoles, resulting in a very high effective ϵ_r', known as colossal permittivity. The phenomenon is said to be temperature-dependent; higher temperatures provide charge carriers with more thermal energy, upsurging their mobility and enhancing charge accumulation at the interfaces. Therefore, Fig. 9 clearly demonstrates this pattern, displaying 3D surface plots of the dielectric constant of Ag → CoNiZnCu (x ≤ 0.10) NSFs across various frequencies and temperatures.

For all surveyed substitution ratios, the characteristics of MW interfacial polarization become evident: the ε_r' is very high at lower frequencies and elevated temperatures and then declines stepwise with increasing frequency.

The main focus of this investigation is on the effect of Ag-substituted NSFs. The results indicate that the unsubstituted NSF (x = 0.00) has a significantly lower ϵ_r' value than any of the Ag-substituted NSFs, while all of the substituted NSFs (i.e., for x ≥ 0.02) demonstrate true colossal permittivity (with $\ln(\epsilon_r') > 10$, indicating $\epsilon_r' > 20{,}000$). These notable

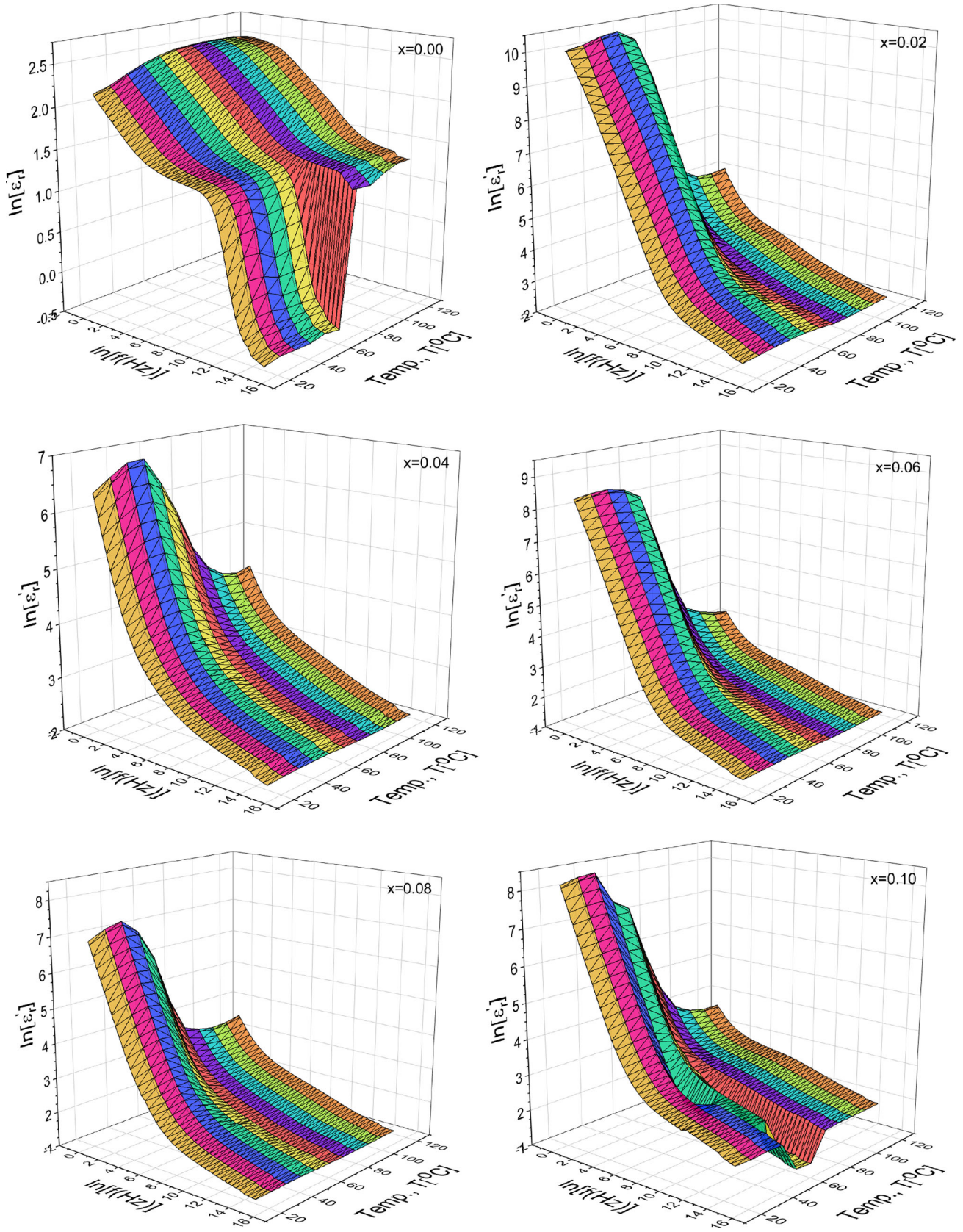

Fig. 9 3D representation of the dielectric constant of Ag → CoNiZnCu (x ≤ 0.10) NSFs

differences are linked to the electrical conductivity of the NSF, as previously noted.

This correlation is explained by the needs of the MW mechanism. There is a very low σ_{DC} for the unsubstituted (x = 0.00) NSF, indicating that there are not enough mobile charge carriers to migrate to and accumulate at the grain boundaries to create interfacial polarization. The sharp rise in both σ_{AC} and low-frequency ε'_r after substitution with Ag ions (x = 0.02) indicates that the addition of a substitute provides more charge carriers to support the polarization process. This suggests that by substituting Ag ions, a system with enough mobile charge carriers and effective blocking barriers to produce colossal permittivity was created.

It is interesting that ϵ_r' reaches its highest point at the x = 0.02 composition, and for higher Ag ion substitution ratios, it decreases to lower values. This trend mirrors the pattern seen in σ_{DC}. This suggests a maximum limit on interfacial polarization. In fact, increasing substitution levels up to x = 0.02 enhances this effect, whereas beyond that, it likely increases the conductivity of the effective blocking barriers themselves, making them 'leaky. When the boundaries of effective blocking barriers no longer hinder charge carrier movement, these carriers will pass through rather than accumulate at the interface. This reduces the magnitude of interface polarization, leading to a decrease in the effective ϵ_r' value.

In summary, MW interface polarization primarily affects the dielectric properties of the ferrite materials under investigation, as demonstrated by the very high ϵ_r' values in Ag ion-substituted NSF systems. ϵ_r' is directly related to the electrical conductivity of NSF. Incorporating Ag ions effectively modifies the relationship between ϵ_r' and electrical conductivity, especially at x = 0.02. At this substitution level, the NSF achieves an optimal state by increasing mobile charge carriers while maintaining high grain boundary resistivity, thereby maximizing the overall charge storage capacity.

3.3.2 *Dielectric Loss (ϵ_r'')*

The response of an NSF to an AC electric field involves both energy storage, characterized by ϵ_r', and energy dissipation, characterized by dielectric loss (ϵ_r''). These phenomena are interconnected; ϵ_r'' is characteristically related to σ_{AC} by the equation $\sigma_{AC}(\omega) = \omega\epsilon_0\epsilon_r''(\omega)$, where ω is the angular frequency, and ϵ_0 is the permittivity of free space [37]**.** Essentially, ϵ_r'' signifies the energy dissipated per cycle and is the physical origin of the frequency-dependent σ_{AC}.

Two primary mechanisms give rise to ϵ_r'' in NSF: (1) Conduction losses, which result from the "long-range" motion of charges and are associated with σ_{DC} in the NSF. These losses usually dominate at low frequency and high temperature. (2) Relaxation losses caused by the inability of the polarization mechanism to keep up with the alternating electric field. This mechanism creates a broad peak in the ϵ_r'' spectrum, which is characteristic of dielectric relaxation. With thermal activation phenomena such as MW interfacial polarization, which we previously discussed, as the temperature increases, the peak position in the ϵ_r'' spectrum shifts to higher frequencies because the characteristic relaxation time of the charge carriers decreases.

The dielectric losses of the Ag → CoNiZnCu (x ≤ 0.10) NSFs were plotted as a 3D surface. As shown in Fig. 10, these materials clearly exhibit the two previously mentioned features. At lower frequencies, the sharp rise in losses is due to increased conduction losses. This trend is further enhanced by the addition of broad relief peaks associated with the MW mechanism; these peaks systematically move toward higher frequencies as the temperature increases, clearly confirming their thermally activated behavior. Therefore, this peak marks the point of maximum energy absorption, and it is evident that it arises when the external field frequency matches the average hopping rate of charge carriers at grain boundary interfaces.

The ϵ_r'' spectra confirm a unified pattern of the electrical properties of NSF materials. The frequency distribution observed in σ_{AC} can be explained physically: The experimental Jonscher power law is known to describe the overall effect of both low-frequency conduction loss (corresponding to the σ_{DC} plateau) and high-frequency relaxation loss peaks. Additionally, the same MW mechanism that produces the enormous ε_r' (energy storage) can also be the source of these relaxation peaks (energy dissipation) and therefore is expected to represent two aspects of the same fundamental phenomenon.

The ϵ_r'' analysis is known to support a combined model explaining how Ag ion substitution affects NSF. First, pure NSF (x = 0.00) exhibits a broad, weak relaxation peak with very low amplitude. Subsequently, when Ag ions are added to NSF (approximately x = 0.02), the amplitude of this relaxation peak increases significantly and appears much sharper than shown by the raw data. Therefore, this observation confirms that Ag substitution increases both the number and mobility of charge carriers, thus strengthening the MW interface polarization. Consequently, the σ_{DC} value increases, leading to a higher ϵ_r' and a more pronounced ϵ_r'' peak. All electrical measurements consistently show a non-monotonic trend reaching a peak at x = 0.02.

In summary, the ϵ_r'' spectra of this ferrite confirm the presence of thermally activated MW dielectric relaxation. The analysis also strongly suggests that the observed loss peaks are the primary mechanism of energy distribution and that σ_{AC} influences the frequency dependence. Additionally, similar results obtained across all four measurement methods (σ_{AC}, σ_{DC}, ϵ_r', and ϵ_r'') provide a unified and consistent explanation. This model explains all electrical behaviors as a consequence of electron hopping within a composite

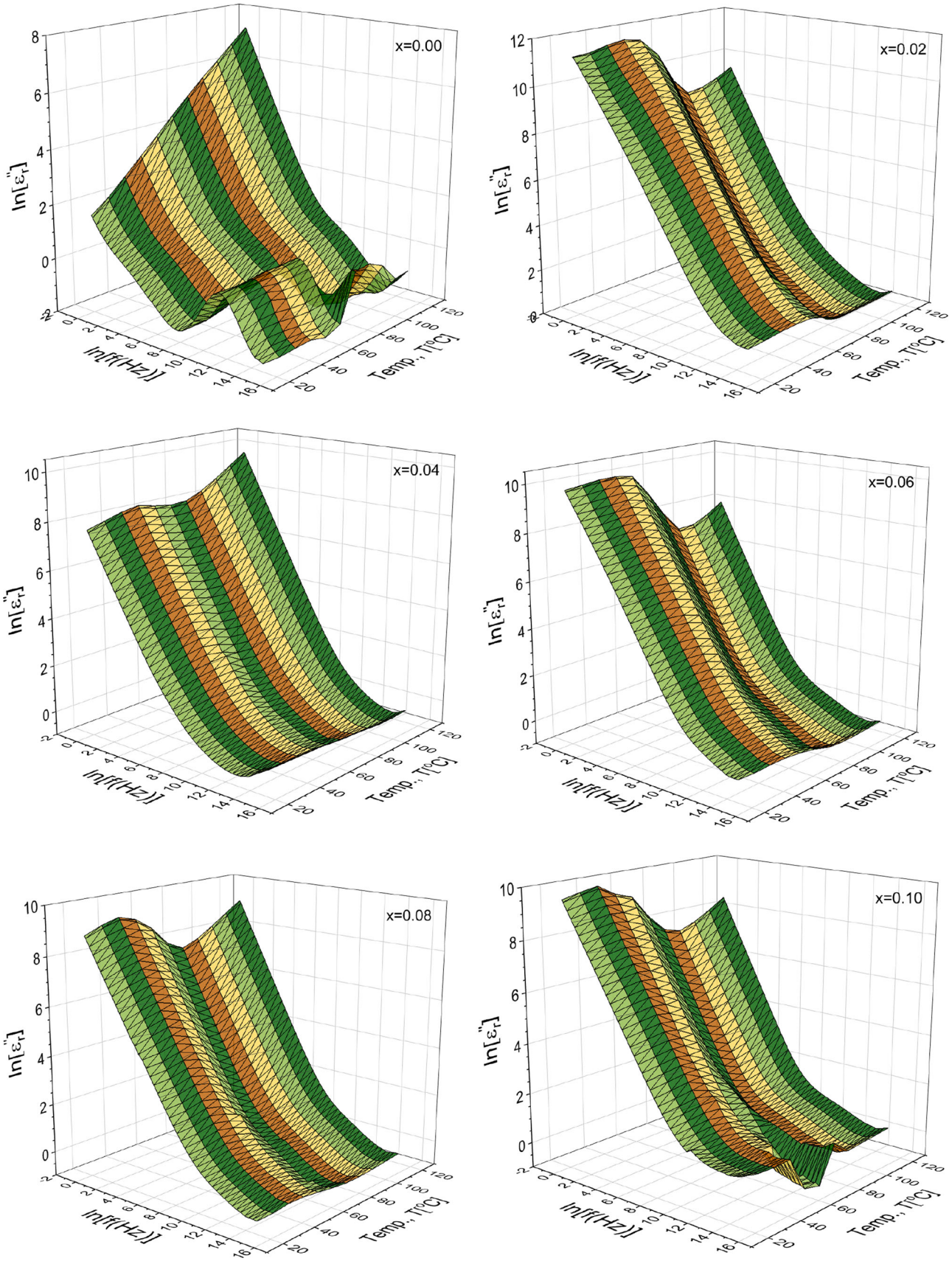

Fig. 10 3D demonstration of the dielectric loss of Ag → CoNiZnCu (x ≤ 0.10) NSFs

microstructure, which can be systematically and predictably managed through Ag^+ ion substitution.

3.3.3 Dissipation Factor (tanδ)

The loss tangent (also called dissipation factor) is a significant parameter for evaluating a dielectric material (NSF). It measures the ratio of energy dissipated to energy stored in an alternating electric field. This factor is defined as $\tan\delta = \epsilon_r'' / \epsilon_r'$, where ϵ_r'' is dielectric loss and ϵ_r' is the dielectric constant, and so, it provides intuition into the behavior of NSFs in this manner.

Figure 11 shows 3D plots of tanδ for Ag → CoNiZnCu ($x \leq 0.10$) NSFs. These graphs disclose peaks associated with relaxation phenomena that shift to higher frequencies with increasing temperature, implying a thermally activated relaxation process. These peaks designate high confidence in the physical model, which was developed based on previous analyses. The relaxation process is attributed to MW interfacial polarization, resulting from the differing structures of conductive grains and resistive grain boundaries [37, 38]**.** The tanδ peaks, where energy dissipation is most competent relative to energy storage, occur at a frequency that exhibits resonance between the applied electric field and the accumulation time of charge-carrier at the grain boundary.

It is important to note that the effect of substituting Ag^+ ions into NSFs on tanδ is clearly marked. **Moreover,** unsubstituted ($x = 0.00$) NSFs display a weak and broad relaxation without a peak. In contrast, NSFs substituted with Ag ions ($x = 0.02$) show much sharper and more intense peaks, indicating an increased energy dispersion due to the Ag ion substitution. This supports the conclusion that Ag ions increase the number of charge carriers and thus improve the interfacial polarization, showing better charge transport along the grain boundaries, as demonstrated in the σ_{DC} data.

As is known, dissipation factor analysis allows all electrical measurements to be combined within a single and consistent framework. The first stage of these measurements is the thermal activation of electrons hopping from one Fe ion (Fe^{2+}) to another one (Fe^{3+}).

- DC conductivity analysis reveals that Ag ion substitution significantly improves the conductivity of grain boundaries by increasing the activity of these mobile ionic charges.
- Dielectric constant analysis indicates that the increased charge activity leads to a significant charge accumulation at the interfaces, resulting in a large amount of energy storage or real permittivity.
- Dynamic measurements of this charge accumulation were conducted using dielectric loss and frequency-dependent conductivity analyses, revealing that the relaxation of this interface charge is a significant energy dissipation mechanism controlling the AC conductivity.
- The dissipation factor strongly supports this correlation. Specifically, it is important to recognize that conditions causing high permittivity (high ϵ_r') also lead to a very high tanδ or a prominent relaxation peak, clearly indicating an increased level of polarization involved in energy dissipation.

The dissipation spectra confirmed that MW interfacial polarization as the foremost contributing factor to the electrical behavior of NSFs, and the detailed dataset shows strong agreement between them. Furthermore, Ag ion substitution significantly affects the NSF microstructures by influencing the electrical properties of the grain boundaries, thereby enhancing interfacial polarization and increasing the dielectric constant, energy loss, and overall conductivity of the NSFs. This helps in understanding how to control the electrical behavior of such complex oxides.

3.4 Complex Electric Modulus Analysis

$M* = 1/\epsilon* = ReM + jImM$ is an analytical framework known as the electric modulus formalism, which is frequently used to examine the dielectric characteristics of NSFs. The main advantage of the electric modulus method is its ability to reduce interference caused by electrode-polarization effects on the dielectric response at low frequencies. This enables a better interpretation of grain relaxation processes in NSFs [37, 40–42]**.**

3.4.1 Real Electric Modulus [ReM vs ln(f)]

As can be seen from the relevant graphs, the frequency characteristic of ReM is typically S-shaped and exhibits a sigmoid distribution. ReM is almost zero at the lowest frequencies; this is known as an indication that charge carriers are mobile over large distances. As the frequency increases, ReM approaches a maximum value (ReM^{∞}) corresponding to ε_r', which is the inverse of the maximum high-frequency electric field polarizability ($ReM^{\infty} = 1/\varepsilon_r^{\infty}$). In the high-frequency range, ReM remains constant because charges cannot respond quickly to rapidly changing electric fields (inductive response). The transition between these two phases (low and high frequency) is called the dielectric relaxation phase. The shift of this transition toward higher frequencies at elevated temperatures suggests that the relaxation rate accelerates with increasing temperature, following an Arrhenius dependence.

3D-plotted graphs (Fig. 12) illustrate the general patterns observed when using Ag ions to substitute ions in the CoNiZnCu NSF system (for $x \leq 0.1$). The 3D surface plots

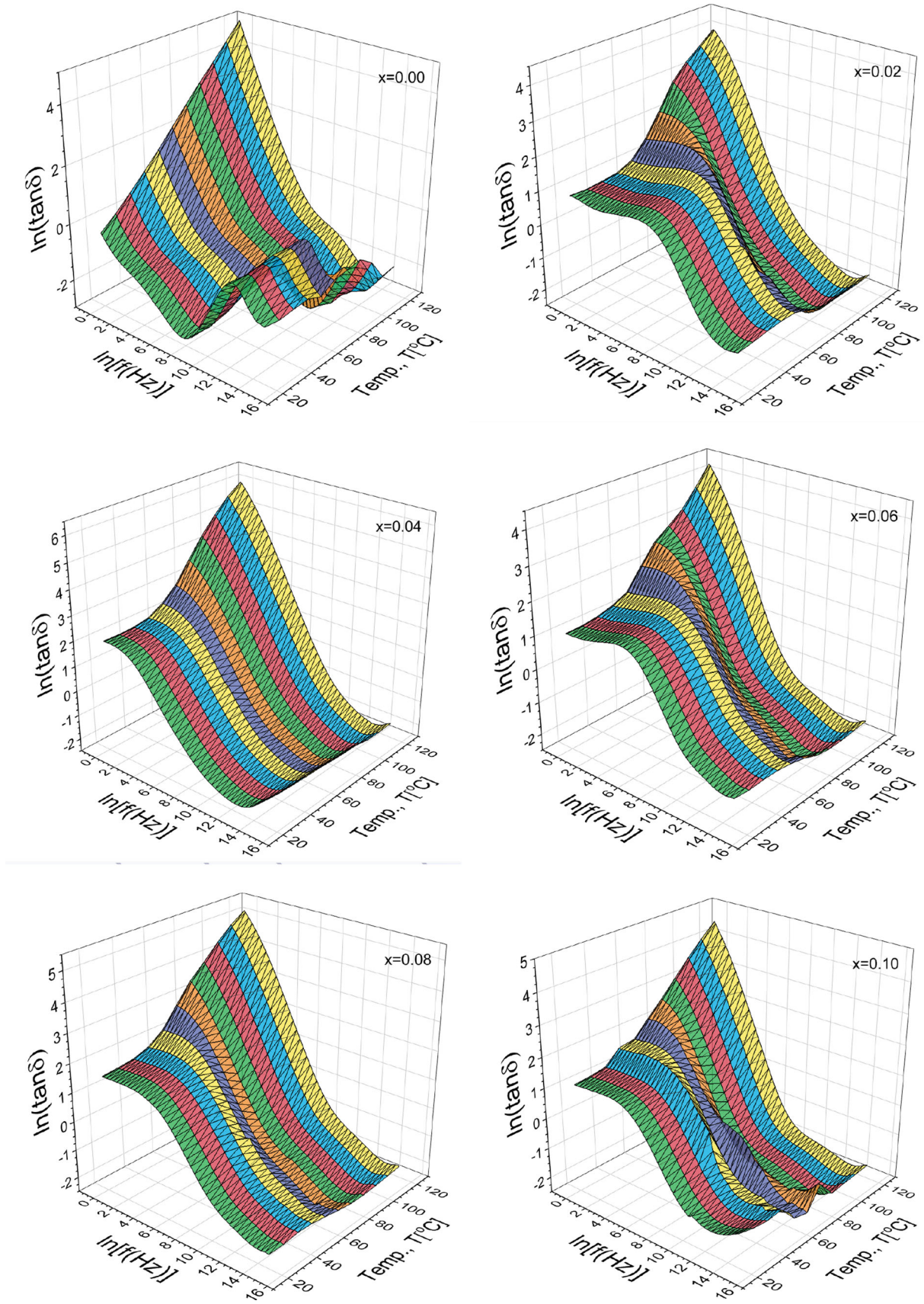

Fig. 11 3D depiction 3D representation of the dissipation factor of Ag → CoNiZnCu (x ≤ 0.10) NSFs

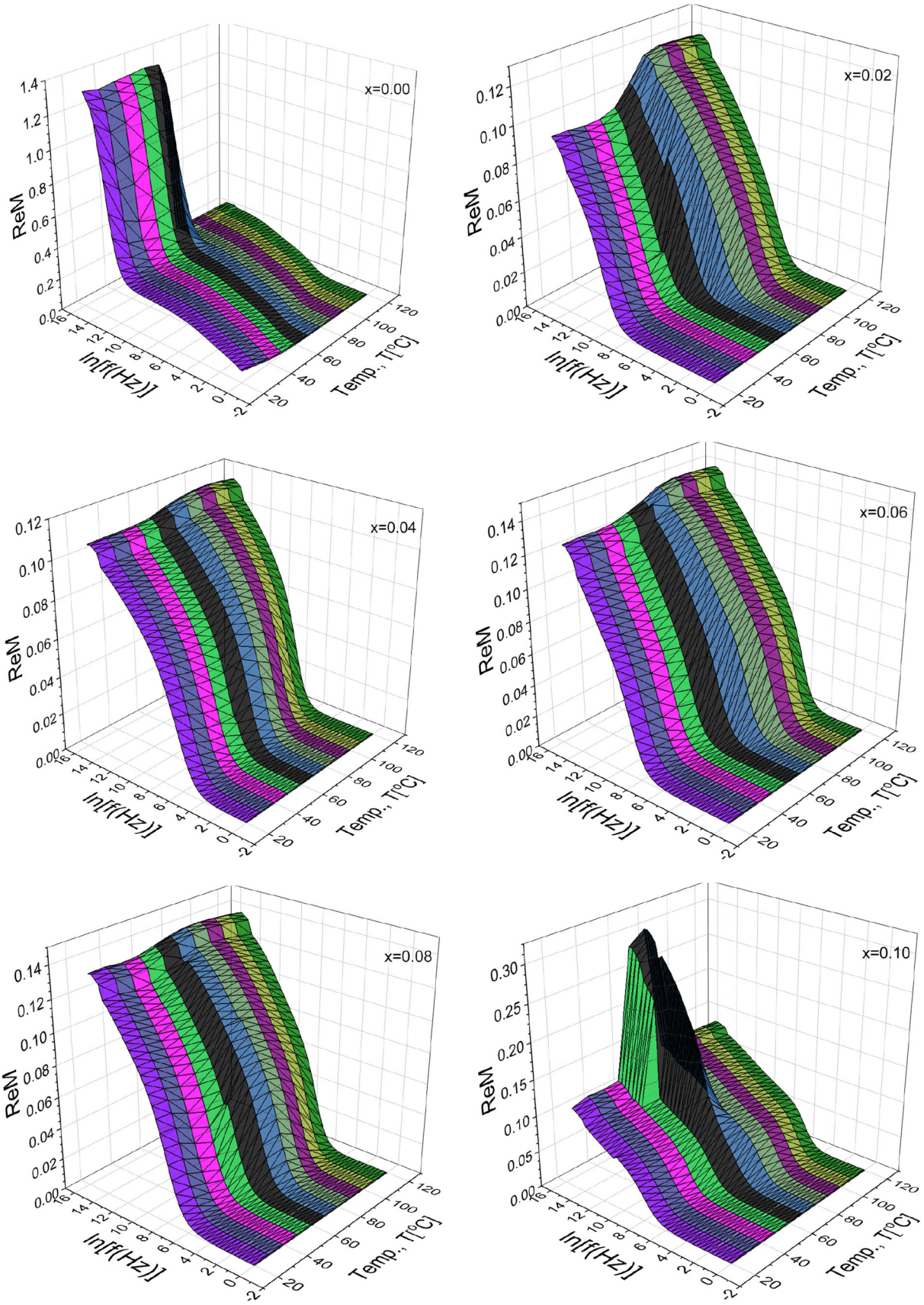

Fig. 12 3D representation of the electric real modulus (ReM) of Ag → CoNiZnCu (x ≤ 0.10) NSFs

from the graph suggest that substituting Ag ions has a non-linear, significant impact on the dielectric properties of the NSF. Using a comparative approach, the extent of this influence can be assessed by considering the different values of x used in the substitutions.

Initially, the baseline for the host NSF (x = 0.00) has a ReM (*the ratio of the material's conductivity to its total charge/carrier)* of about 1.2–1.3, indicating a high level of charge mobility. The host compound is also characterized by a low value of the high-frequency dielectric constant ($\epsilon_r{}'^{\infty}$).

Then, at low substitution levels (x = 0.02 to x = 0.08), a dramatic shift occurs. A small amount of Ag ion greatly reduces the maximum ReM value within a stable range of approximately 0.12–0.14. This corresponds to about a ten-fold increase in the intrinsic dielectric constant of ϵ^{∞}. This enhancement results from the chemistry of NSFs. In this type of ferrite, electronic polarization happens through the hopping of electrons between Fe^{2+} and Fe^{3+} ions. Introducing Ag^{+} (*monovalent*) to substitute Fe^{3+} (*trivalent*) requires charge compensation, which likely causes the formation of additional Fe^{2+} ions. As a result, the higher concentration of polarizable $Fe^{2+} - Fe^{3+}$ ion pairs significantly boosts the bulk polarizability of the NSF, leading to an increase in ϵ^{∞} and a decrease in M^{∞}.

The substitution trend shifts at high substitution levels (x = 0.10), where a new manner emerges, with ReM near zero. It should be noted that the ReM peak reaches approximately 0.30, indicating a decrease in the grain $\epsilon r'$ value compared to intermediate ratios. Specifically, a sharp, resonance-like peak appears at low frequencies and high temperatures; this is unusual for grain relaxation and points to a fundamental change in the electrical response of NSF. Possible reasons for this are: firstly, interfacial polarization due to Ag^{+} ion deposition at grain boundaries affecting the response; or secondly, phase decomposition occurring if the solubility limit of Ag within the spinel structure is exceeded.

Overall, electrical modulus analysis shows that the dielectric properties of these ferrite grains can be tuned through the substitution of Ag ions. While NSF generally exhibits thermally activated dielectric relaxation, it is common for the substitution effect to be non-monotonic. Small amounts of Ag (x ≈ 0.02) are thought to significantly increase the intrinsic $\epsilon_r{}'$ value, possibly due to the increasing Fe^{2+}/Fe^{3+} ratio. At higher Ag levels (x = 0.10), this grain effect may be replaced by a novel mechanism, possibly arising from changes in grain boundaries or phase decomposition, indicating a fundamental change in the electrical structure. This complex behavior highlights the critical influence of the substitution ratio on the design of the dielectric response of NSFs.

3.4.2 Imaginary Electric Modulus [-ImM vs ln(f)]

It is well known that ImM provides a different perspective from ReM by revealing how energy dissipates in the NSF. The ImM spectrum displays peaks that identify dielectric relaxation processes, and the position of each peak in frequency indicates when a relaxation process occurs. The peak frequency (f_{max}) is inversely related to the most likely relaxation time (τ); that is, $2\pi f_{max}\tau = 1$.

A 3D surface graph displaying 'ImM' as a function of concentration for Ag → CoNiZnCu (x ≤ 0.10) NSFs is presented in Fig. 13**.** Regarding the Ag ion substitution ratio within the NP structure, two clear characteristics are observed across all substitution levels. First, at higher temperatures, the relaxation peak frequency shifts to higher values, reflecting the thermally activated behavior of charge-carrier mobility. Second, the relaxation peak is broad across all substitution ratios, indicating a wide range of relaxation times associated with charge carriers in a highly complex, structurally and electrically heterogeneous material.

The main benefit of ImM analysis lies in its capacity to clarify and confirm the non-monotonic influence of Ag ion substitution on ReM data. By analyzing energy-dissipation features, we gain a deeper understanding of these effects than by using ReM data alone. The unsubstituted NSF (**x = 0.00**) exhibits a single, highly intense, and broad relaxation peak, peaking around 0.5. The intensity and width of the peak suggest a grain relaxation process that encompasses a broader range of relaxation times than the typical host NSF.

At low substitution levels, with x from 0.02 to 0.08, the substitution of Ag ions led to a significant decrease in the relaxation peak's intensity, which then plateaued around 0.03. This indicates that initial Ag^{+} ion incorporation significantly altered the charge carriers' environment; the NSF was expected to exhibit a much higher intrinsic ε_r' (according to ReM), yet it would experience less energy loss through this primary relaxation channel. Notably, the NSF with x = 0.04 showed a shoulder on the low-frequency side, implying the formation of multiple relaxation mechanisms, possibly involving decoupled grain and grain boundary contributions.

The regime with a high substitution ratio (x = 0.10) shows the same unusual trends previously discussed regarding the ReM analysis and displays perhaps the most extreme relaxation peak observed to date, with an intensity significantly higher than that of the NSF, which was replaced with an intermediate amount of material. The location of this peak in the low-frequency, high-temperature region precisely aligns with the resonance-like feature observed in the ReM plot.

By analyzing the combined ReM and ImM datasets, it is evident that they strongly support the presence of this abnormality. The dissipation peaks in ImM spectra match the dispersion peaks in ReM spectra (Kramers–Kronig relationships) [25, 26]. The most prominent feature of the new peak

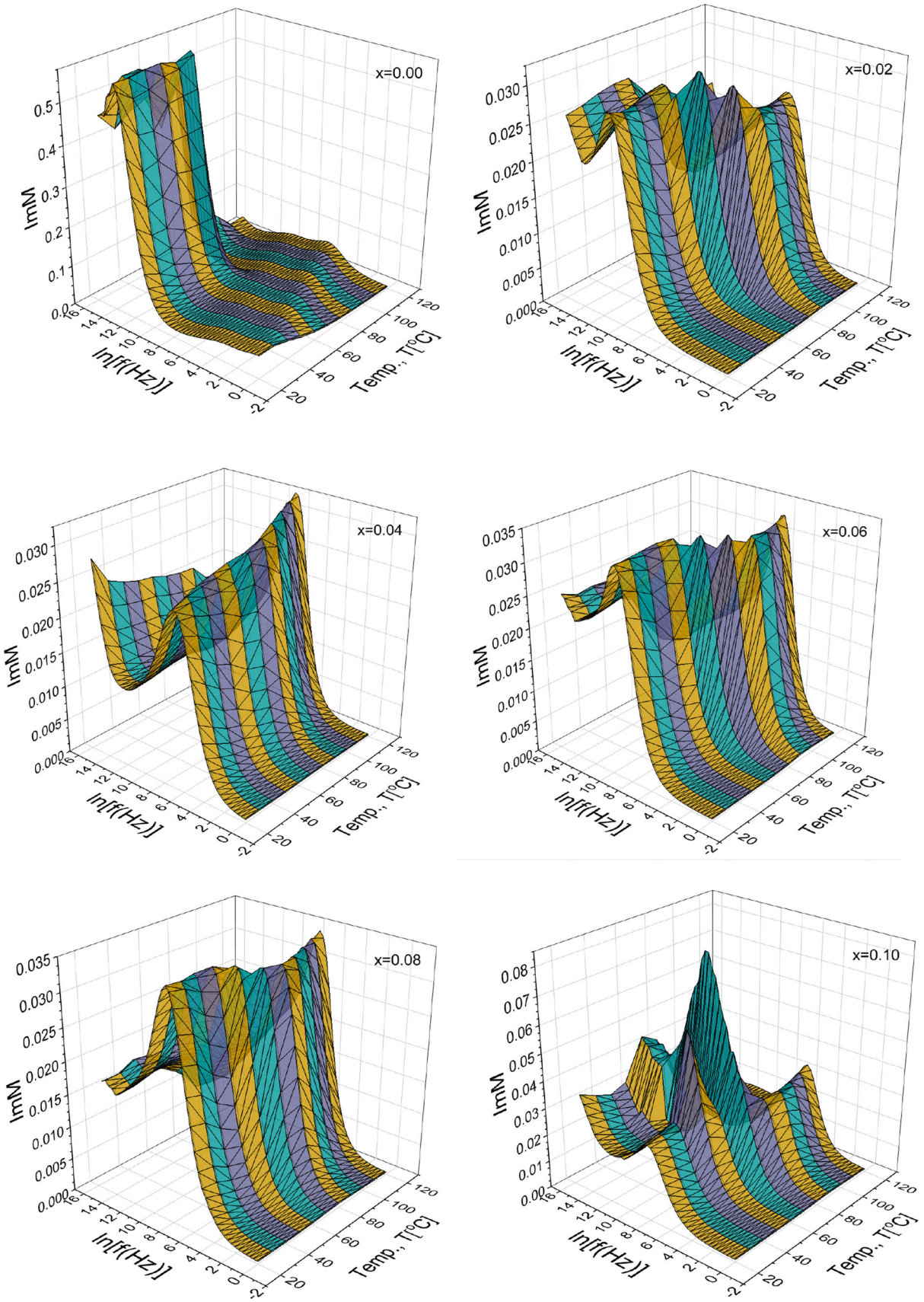

Fig. 13 3D illustration of the imaginary modulus (-ImM) of Ag → CoNiZnCu (x ≤ 0.10) NSFs

at a substitution ratio of x = 0.10 is its sharpness; unlike typical grain relaxation processes that extend over wider ranges, this narrow peak indicates an electrical event with a coherent relaxation time in that region and a specific electrical mechanism.

The most likely elucidation is that at higher substitution ratios (i.e., x = 0.10), Ag^{+} ions accumulate at grain boundaries, forming a boundary with properties different from the grains. This accumulation likely causes a pronounced interfacial polarization effect, leading to a prominent resonant dissipation peak in the modulus spectrum [38].

In summary, it should be well understood that the analysis of the combined electric modulus (both ReM and ImM) confirms that thermally activated dielectric relaxation causes dual functionality associated with substituent Ag ions. Specifically, below x = 0.10, Ag should control the intrinsic relaxation of the grains by altering the Fe^{2+}/Fe^{3+} ion ratio. Above x = 0.10, it is noteworthy that a new, clear interface process emerges, leading to significant changes in dielectric relaxation. It should be emphasized that the ImM analysis clearly demonstrates that this new mechanism is an enhanced form of interface polarization, driven by well-defined, Ag-modified grain boundaries. It is also important to highlight how the substituent substitution can significantly alter both the strength and character of the dielectric response in complex oxides.

3.4.3 Complex Electric Modulus: Nyquist Plots (-ImM vs ReM)

The electric modulus formalism, shown as a Nyquist plot (-ImM vs ReM), is useful for differentiating the electrical contributions of the grains and grain boundaries in an NSF. As depicted in Fig. 14**,** Ag → CoNiZnCu (x ≤ 0.10) NSFs at temperatures ranging from 20 to 120 °C provide clear indication that supports a comprehensive understanding of the electrical characteristics of the NSF.

It is well known that a dielectric relaxation process depicts a semicircular shape, while a depression on the ReM at lower frequencies reveals a dispersion of relaxation times typical of non-Debye relaxation [37]**.** Thus, the broad peaks in the frequency plot reinforce this, which is common given the structural inhomogeneities in NSFs. Moreover, as the temperature rises, the arcs shrink, indicating that the dielectric and conductive properties are thermally activated.

Furthermore, the gradual changes observed in these Nyquist plots as Ag ion substitution increases are visually consistent with all previous conclusions and help link the findings. The unsubstituted NSF (x = 0.00) demonstrates a single dominant relaxation process, exposed by one large semicircular depression in the Nyquist plot. In this scenario, the high resistance of the grain boundaries obscures the electrical response of the lower-resistance grains, yielding a single primary impedance response, and alternatively, introducing Ag ions significantly modifies the structure and properties of the NSF.

The broad arc degenerates into a much smaller arc at x = 0.02, shifting the high-frequency intercept on ReM from approximately 1.25 to 0.12. This significant change appears to support the previously calculated increase in the high-frequency dielectric constant ($\epsilon_r{}'^{\infty} = 1/\mathrm{ReM}^{\infty}$) observed from the 3D modulus graphs. Consequently, for the intermediate substitution ratios of x = 0.04 and 0.06, a secondary, less distinct arc begins to emerge on the low-frequency edge of the main semicircle. In this case, recognizing these two separate arcs is important; the direct experimental evidence of the heterogeneous electrical behavior of NSFs is significant. This deconvolution is the usual case, demonstrating that Ag substitution sufficiently reduces grain-boundary resistance and that the electrical response of the grain boundaries is distinguishable from that of the grains.

At a highest substitution ratio of x = 0.10, the characteristic tendency of NSF is clearly observable. The plot shows that, at higher temperatures, the two semicircles resulting from this substitution become clearly distinguishable. Although at lower frequencies the lower semicircle includes some contribution from grain responses, the larger arc at these frequencies indicates the contribution from grain-boundary responses. The presence of both semicircles is typical of MW systems, confirming interfacial polarization and strongly supporting the idea that Ag^{+} ions accumulate at grain-boundary interfaces when the substitution level is high [38].

Moreover, the analysis of the electrical characteristics of the ferrite system presents a single, self-consistent physical model for how ferrite systems behave electrically. Electrical responses are thermally activated by hopping electrons through the discontinuous microstructure (*due to random spatial positions*) of the NSF, while frequency-dependent electrical behavior is shown to be represented by an Interfacial Polarization Model (MW model). Evidence supporting this MW model can be found in the Nyquist plots of the complex moduli. These figures represent the electrical responses of the grain and the grain boundary. The systematic work has demonstrated that Ag substitution is the most effective mechanism for adjusting the electrical properties (including NSF) of ferrite, as it has been shown to reduce grain-boundary resistivity. All other phenomena observed can be attributed to this single microstructural modification of increasing σ_{DC} (*electrical conductivity*), the colossal $\epsilon_r{}'$, and the pronounced relaxation effects, which clearly demonstrate that all the dielectric and electrical properties of the ferrite are dependent on the discontinuous microstructure of this ferrite, which can be shaped through targeted chemical substitution.

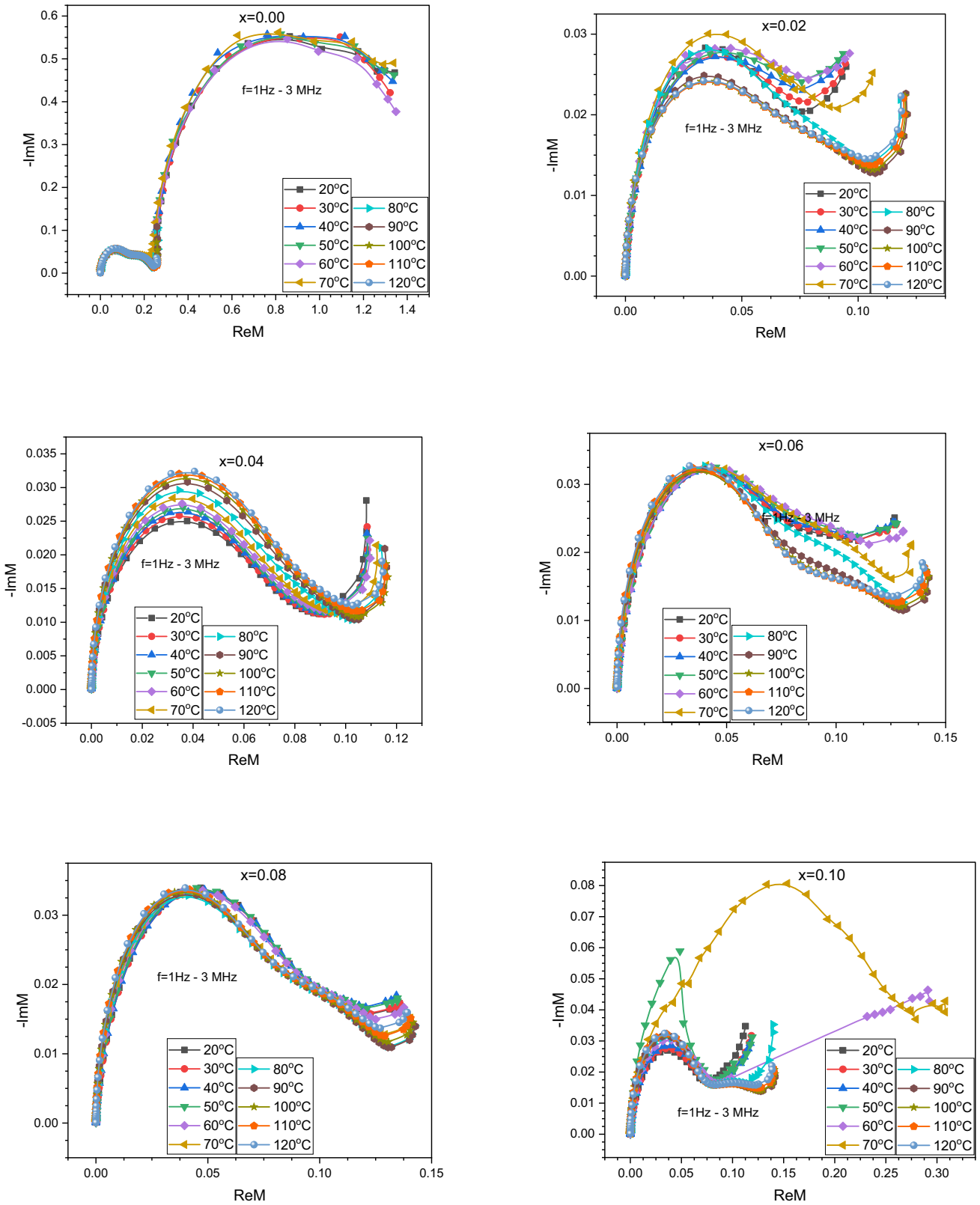

Fig. 14 Nyquist plots of the complex electric modulus (-ImM vs. ReM) of Ag → CoNiZnCu (x ≤ 0.10) NSFs

3.4.4 Maxwell–Wagner Methodologies

The noticed dielectric performance is enlightened within the framework of M–W interfacial polarization, which is strongly validated by merged analyses of dielectric loss, dissipation factor, and electric modulus. It is evident that the ε_r'' spectra exhibit a strong improvement at low frequencies due to conduction losses at grain boundaries, along with extensive relaxation peaks that shift systematically to higher frequencies with increasing temperature. This thermally activated shift approves that the relaxation process surveys Arrhenius-type behavior and originates from interfacial polarization mechanisms.

Similarly, the tanδ spectra present clear relaxation peaks whose positions shift to higher frequencies as the temperature rise up, satisfying the condition $\omega\tau \approx 1$. These peaks designate charge carrier buildup and release at grain boundary interfaces, providing direct evidence of MW polarization.

Further validation was obtained from complex electrical modulus analysis ($M^* = ReM + jImM$). The ImM spectra reveal the distribution of relaxation times and broad relaxation peaks indicating non-Debye behavior. Suppression of electrode effects in the modulus formalism allows for clear characterization of grain-related relaxation processes, as the emergence of multiple features at higher Ag^+ ion substitution ratio suggests a separation of grain and grain boundary contributions.

The relationship among the ε_r', ε_r'', tanδ, and ReM/ImM spectra indicates that the enormous dielectric constant or colossal permittivity ($\varepsilon_r' > 10^4$) arises from interfacial charge accumulation in a heterogeneous microstructure consisting of both conductive grains and resistive grain boundaries. At a low Ag^+ ion substitution ratio ($x \approx 0.02$), the optimum balance between carrier concentration and grain boundary resistance results in maximum interfacial polarization. At higher substitution ratios, increased grain boundary conductivity reduces charge accumulation (leakage barrier effect), thus decreasing the dielectric constant [43, 44].

Consequently, the combination of the frequency- and temperature-dependent behavior of the dielectric loss, relaxation peaks, and modulus spectra provides strong experimental evidence that the observed enormous dielectric constant is predominantly governed by M–W interfacial polarization rather than purely intrinsic polarization mechanisms [43].

3.5 Complex Impedance Analysis

3.5.1 Real Impedance [ReZ vs ln(f)]

Charge-transport mechanisms can be further analyzed using the real part of the complex impedance (ReZ) of the NSF, which indicates the overall resistivity. Figure 15 shows how ReZ varies with frequency for the Ag → CoNiZnCu (0×0.10) NSFs at different temperatures.

ReZ frequency response characterizes NSFs across all compositions. At low frequencies, ReZ reflects the total DC resistance (R_{DC}) of the NSFs, forming a constant plateau. As frequency increases, ReZ sharply drops and stabilizes at a much lower value, which corresponds to R_G—the resistance of individual bulk grains—since the bulk grains have much higher resistances than the grain boundaries. Grain boundaries primarily exhibit resistance to direct current and control the resulting response; at higher frequencies, the capacitor becomes more functional and shows a tendency toward short-circuiting. Additionally, the temperature dependence of ReZ shows a significant decrease with increasing temperature across all NSFs, which is consistent with previous studies on NSFs and confirms their thermally activated semiconductor behavior.

The most important finding of this study is how Ag ion substitution strongly affects the resistance of NSF. The unsubstituted parent NSF has an extremely high DC resistance in the GΩ range. In contrast, an NSF containing only a small amount of Ag ($x = 0.02$) shows a resistance reduction down to the MΩ range, representing a reduction of more than twofold compared to the unsubstituted version. This clearly demonstrates that the addition of Ag ions greatly reduces the DC resistance of NSFs. Furthermore, grain boundaries, which are the primary limiting conduction pathways, become significantly more conductive due to Ag substitution.

Systematic investigation of the electrical and dielectric properties of Ag → CoNiZnCu ($x \leq 0.10$) NSFs has revealed that they form a coherent and self-sufficient physical framework. The primary charge-transport mechanism in this system is thermally activated electron hopping, as verified by the temperature dependence of the DC conductivity.

The unique microstructure of NSF—comprising conductive grains with resistive grain boundaries—enables a better understanding of its exceptional frequency-dependent properties. This arrangement leads to the formation of MW interfacial polarization, which is the mechanism behind the dielectric response of NSFs.

This research shows that substituting Ag ions can form a new type of microstructure. A major effect of substituting Ag ions into the NSFs was to greatly increase their σ_{DC}, evidenced by a significant decrease in R_{DC} as shown by impedance analysis of the NSFs. The rise in σ_{DC} led to all other observed effects in the NSF material. Due to the increased number of conductive ions in NSF, improvements in MW interface polarization have led to a very low-frequency dielectric response in these substituted NSFs, exhibiting high polarizability and high dielectric responses. It is also clear that the thermally activated relaxation peak in the ε_r'' spectra proves the MW effect [37, 38].

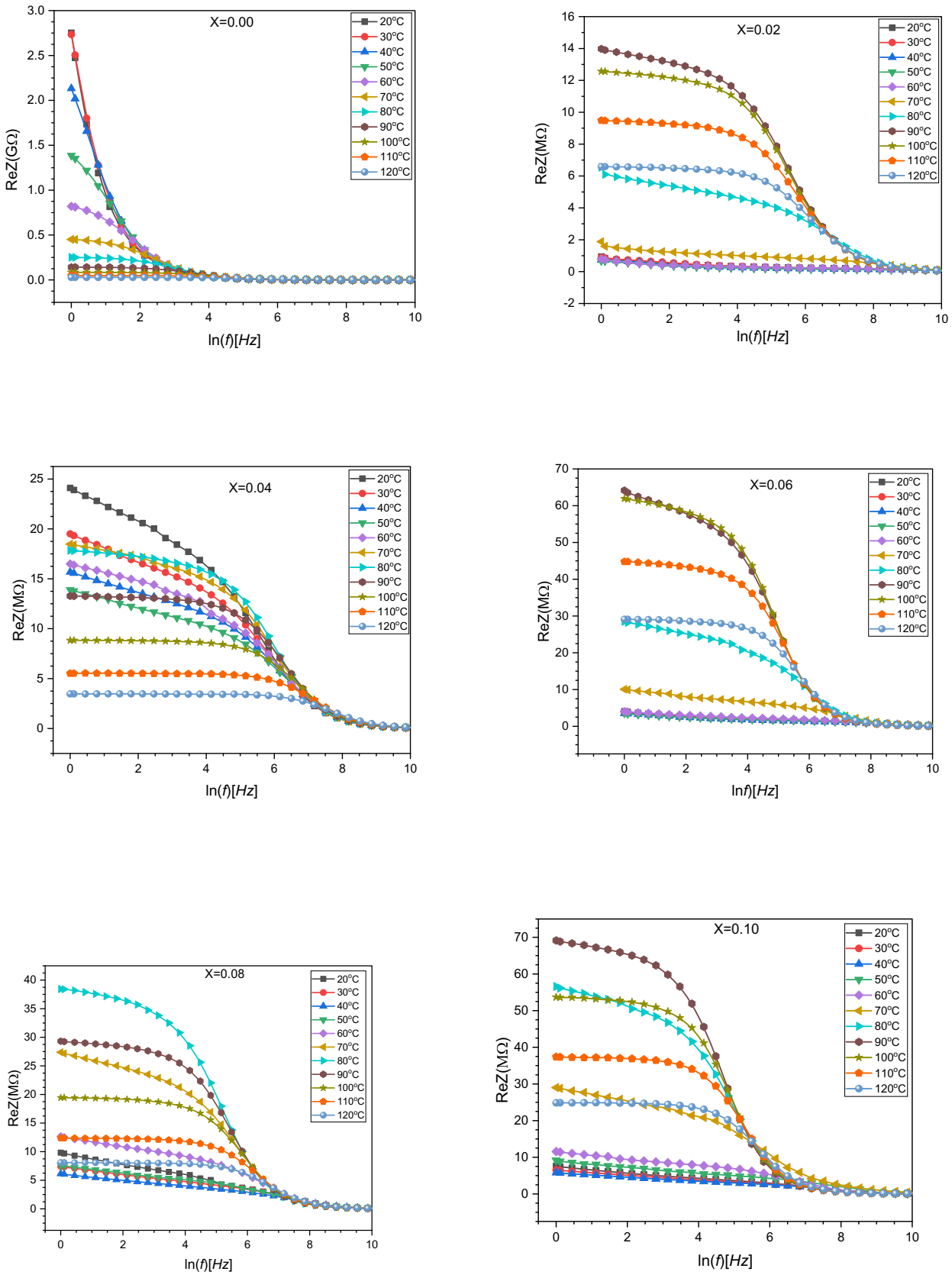

Fig. 15 The characterization of real impedance (ReZ) of Ag → CoNiZnCu (x ≤ 0.10) NSFs

Subsequently, the implemented model has been comprehensively confirmed by examining both the complex electrical modulus and complex impedance, yielding consistent findings. Thus, while the electrical modulus analysis insulates the grain relaxation processes, Nyquist plots graphically exhibit the biphasic electrical behavior of NSF. The evolution from a single large semicircle in unsubstituted NSF to two distinct arcs in substituted one clearly demonstrates that the Ag^+ ion primarily reduces the grain boundary resistance and underlines the intrinsic response of the grains. This comprehensive study confirms that the electrical and dielectric characteristics of this specific NSF with a heterogeneous microstructure can be systematically tuned and improved, primarily through the modification of grain boundary conductivities, via targeted cation substitution with Ag^+ ions.

3.5.2 Imaginary Impedance [-ImZ vs ln(f)]

The ImZ is primarily affected by the resistive components of the complex impedance in NSFs, which is critical in the analysis of energy loss mechanisms. In Ag → CoNiZnCu, [x ≤ 0.10] NSFs, the frequency dependence of the ImZ exhibits distinct relaxation peaks (see Fig. 16). Each peak indicates an enduring relaxation process; the peak frequency links to the maximum energy dissipation and is consistent with the characteristic relaxation time for this process.

For each NSF, as the temperature increases, all spectra corresponding to each of the respective substitution ratios shift toward higher frequencies due to thermal activation. Another common feature of Ag^+ ion-substituted NSFs is the presence of two mismatched peaks simultaneously in their spectra. Accordingly, this becomes more pronounced at higher temperatures compared to lower temperatures. From an impedance perspective, the main characteristic is the largest peak in the impedance curve, representing the resistive elements in the NSF system. As a result, the low-frequency peak is attributed to grain boundaries, while the less resistive area appears as a smaller shoulder at higher frequencies [37, 40–45].

The most important finding from this research was the impact of substitution on the primary ImZ peak, which corresponds to grain-boundary resistance. For non-substituted NSF (x = 0.00), the ImZ peak is around the GΩ range, while for all substituted NSFs, the ImZ peak drops into the MΩ range. This clearly and strongly supports the conclusion that Ag^+ ion substitution significantly decreases grain-boundary resistance, a finding consistent with all previous studies [37, 41–45].

When a comprehensive analysis was carried out using multiple complementary methodologies on the electrical data obtained from Ag-substituted ferrite, it yielded a coherent, self-consistent model of the material. Using σ_{DC} measurements and supporting ReZ data, we validated that thermal activation of electron hopping is the primary charge-transport mechanism.

Understanding the frequency-dependent behavior of the NSF can be attributed to its heterogeneous microstructure, which produces MW interfacial polarization. This study shows that the main purpose of substituting Ag ions into the NSF is to modify its microstructure by significantly reducing the grain-boundary resistivity. This microstructural change caused by Ag substitution is the main reason for all other effects observed in this research. The increase in total conductivity, caused by more mobile charge carriers, leads to enhanced interfacial polarization, which is responsible for the extremely large permittivity and strong dielectric dispersion observed in the Ag-substituted NSFs. The thermally activated relaxation peaks observed through dielectric loss, dissipation factor, and impedance spectra all originate from the same underlying MW process.

Using complementary forms and methods was crucial for establishing the validity of this model. The impedance (ImZ) spectra reveal nearly all of the resistance effects caused by grain boundaries; however, the electric modulus (ImM) spectra suppress this effect, allowing us to clearly observe the relaxation associated with less-resistive grains. Therefore, distinguishing the grain boundary peak from the ImZ spectrum and the grain peak from the ImM spectrum exemplifies a classic and powerful feature of impedance spectroscopy.

Finally, the Nyquist representations of the complex modulus provided the clearest view of the two-phase electrical properties of the NSF. The shift from a single semicircle in the unsubstituted NSF to two smaller semicircles in the substituted NSFs clearly verifies the MW model. Visually, this shows how Ag substitution alters the relative contributions of grain and grain boundary electrical properties. The Ag substitution reduces the grain boundary resistance enough to isolate and characterize the intrinsic response of the grain. Overall, the evidence strongly supports the idea that the electrical and dielectric properties of this complex NSF result from a heterogeneous microstructure that can be influenced by specific chemical substitutions, as mentioned earlier.

3.5.3 Complex Impedance: Nyquist Plots (-ImZ vs ReZ)

The complex impedance Cole–Cole plot, or Nyquist plot, is essential in impedance spectroscopy because it allows for direct visualization of resistive and capacitive components within a NSF. Figure 17 illustrates these Nyquist plots for the Ag → CoNiZnCu (x ≤ 0.10) NSFs.

All NSF spectra exhibit flattened semicircular arcs, characteristic of systems containing parallel resistor–capacitor (RC) circuits. The observed arc flattening suggests a non-Debye relaxation with a range of relaxation times, consistent with the typical structural inhomogeneity of NSF. Additionally, elevating temperature causes a significant drop in the

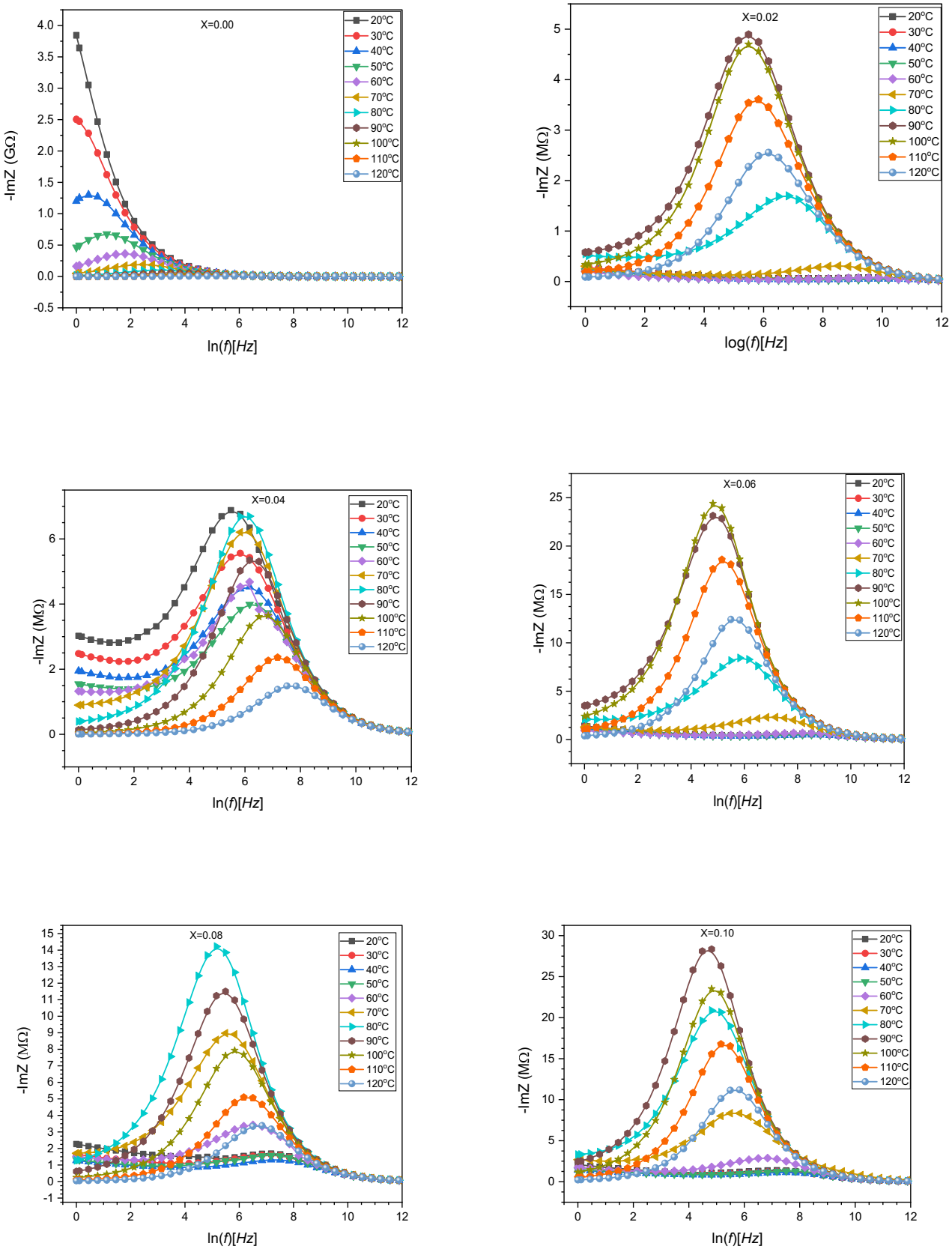

Fig. 16 The characterization of imaginary impedance (-ImZ) of Ag → CoNiZnCu (x ≤ 0.10) NSFs

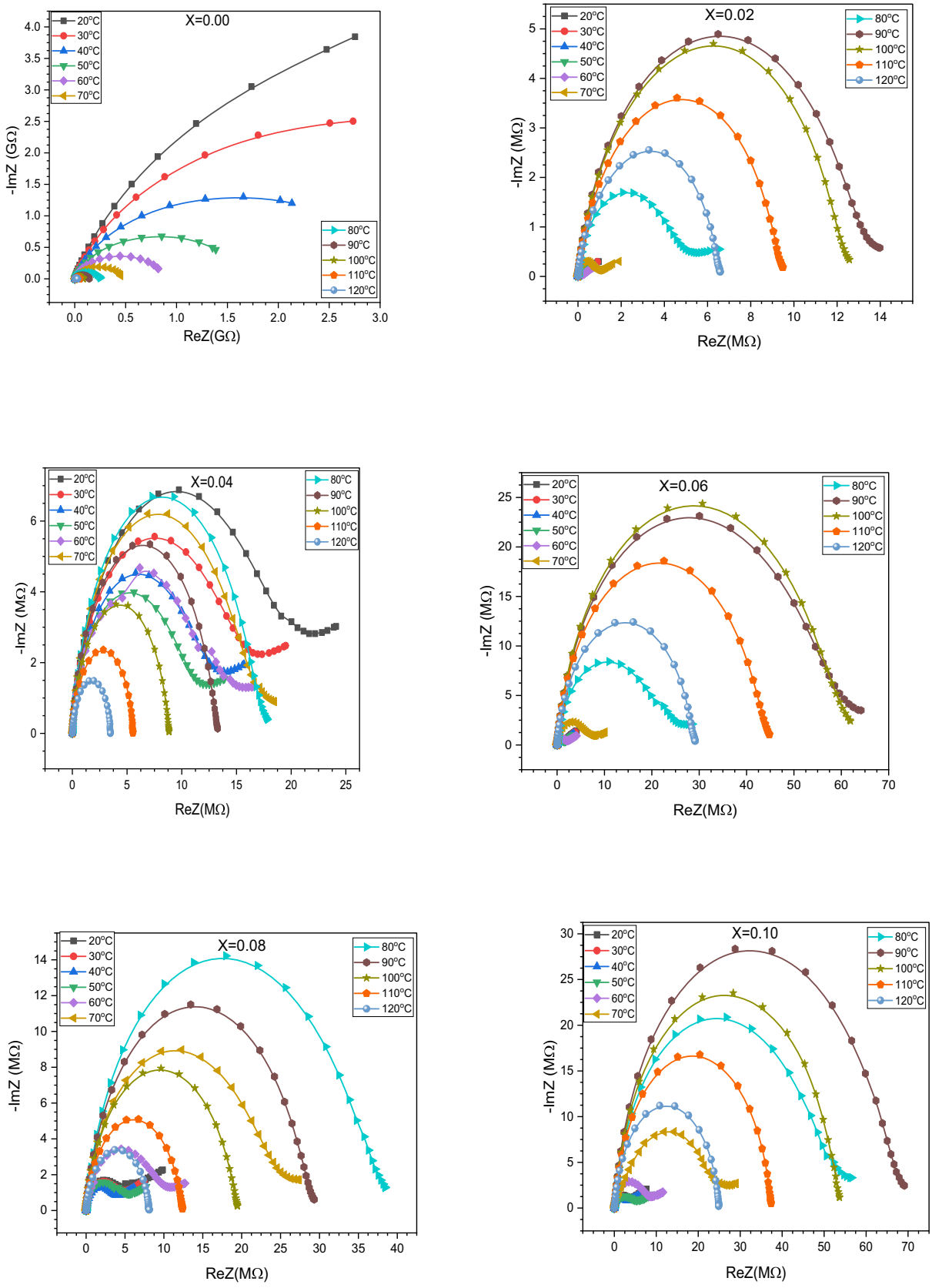

Fig. 17 Nyquist plots of complex impedance (-ImZ vs ReZ) of Ag → CoNiZnCu (x ≤ 0.10) NSFs

diameter of the semicircle, indicating the resistance of the component involved. This visual evidence clearly demonstrates the semiconductor behavior in NSF where resistance decreases with thermal activation.

The fundamental information comes from how the spectra changes with substitution ratio, providing clear evidence of different effects at the grain and grain boundaries. The pure NSF (x = 0.00) illustrates a single, large semicircle of a few GΩs in diameter, indicating that the electrical response is primarily manipulated by the grain boundary, which is a high-resistive component of the complex impedance.

Furthermore, NSFs substituted with Ag^+ ions clearly exhibit two overlapping semicircular arcs, one smaller at higher frequencies and the other larger at lower frequencies. This dual-arc pattern suggests some ceramics with two distinct electrically active regions. The high-frequency arc signifies the grain response, while the low-frequency arc represents the high resistance occurring at the grain boundaries. The transition from a single GΩ-scale arc to two smaller MΩ-scale arcs with Ag^+ ion substitution clearly reveals a significant reduction in grain boundary resistance. Subsequently, the grain response, formerly concealed by the much higher resistance at the grain boundaries, is now readily noticeable.

An inclusive valuation of electrical characterization using various complementary techniques provides an all-inclusive and intrinsically consistent picture of Ag^+ ion-substituted NSF. A thermally activated electron-hopping process, which contributes to the electrical response, occurs throughout the composite microstructure. The high dielectric constant and the associated relaxation effect result from MW interfacial polarization mechanisms [38, 41, 42].

The main goal of Ag substitution is to significantly lower the resistivity of grain boundaries through enhanced interfacial polarization effects, thereby improving grain conductivity. The relaxation process was examined using various techniques, which helped clarify how this process takes place. Dielectric loss spectra confirms that part of the energy dissipation results from the MW process; however, the ImZ and ImM spectra show that the relaxation response can be divided into two distinct responses linked to the grain boundary and grain relaxation peaks, respectively.

In conclusion, the Nyquist plot of both the impedance and modulus formulations provides a clear depiction of how NSF was constructed electrically. The presence of two distinct semicircles indicates that the NSF are heterogeneous and supports the use of the MW model to describe the data presented. The collective information within each plot reinforces the MW model by showing how specific modifications to a polymer using different molecular components can alter the electrical properties of engineered polycrystalline ferrites [45].

3.5.4 Equivalent-Circuit Modeling

The Nyquist plots of Ag → CoNiZnCu, x ≤ 0.10, demonstrate clear semicircular arcs across the 1 Hz–3 MHz frequency range, indicating thermally activated electrical relaxation influenced by heterogeneous microstructural factors, as shown in Fig. 18. It is noteworthy that the appearance of semicircles and deviations from ideal Debye behavior indicates a distribution of relaxation times associated with electrically distinct regions, primarily grains and grain boundaries.

To quantitatively interpret the impedance response, the spectra were fitted using an EEC of the form $R_S(CR)(QR)(CR)$. This EEC model effectively apprehends the heterogeneous electrical contributions of the NSF system. In this section, the series resistance (R_S) firstly signifies electrode/contact effects. Secondly, the high-frequency (CR) element corresponds to the grain contribution, where R_G arises from intrinsic charge transport dominated by Fe^{2+}/Fe^{3+} electron hopping, and C_G reflects grain dielectric polarization. Thirdly, the low-frequency (CR) element is attributed to grain boundary effects, with R_{GB} representing the resistive barrier of insulating interfaces and C_{GB} corresponding to interfacial capacitance associated with MW polarization. Lastly, the intermediate (QR) component incorporates a constant phase element (CPE), which accounts for non-ideal capacitive behavior arising from structural disorder, compositional fluctuations, and spatially distributed relaxation processes. The CPE exponent (n < 1) confirms significant deviation from ideal Debye relaxation and reflects defect-mediated charge transport and interfacial heterogeneity [46].

It is clear that Nyquist profiles strongly support the assignment of circuit elements: the high-frequency arc correlates to grain effects and the low-frequency arc to grain boundary contributions. The depressed character of these arcs further justifies the inclusion of the CPE element. The excellent agreement between experimental and fitted data (Tables 5, 6, 7) confirms that the impedance response is dominated by a coupled contribution of grain resistance (R_G), grain boundary resistance (R_{GB}), interfacial capacitances (C_G, C_{GB}), and non-ideal polarization effects symbolized by the CPE.

It is well known that the substitution ratios of Ag^+ ions significantly alter the electrical parameters at room temperature. In particular, R_{GB} remains significantly higher than R_G, indicating that grain boundaries dominate the charge-carrying resistance. However, the systematic changes observed in R_G, R_{GB}, and capacitance with increasing Ag^+ ion ratio suggest changes in charge carrier density and interfacial polarization. Subsequently, this behavior is attributed to changes in Fe^{2+}/Fe^{3+} hopping channels and defect chemistry induced by Ag^+ ion incorporation, leading to improved electrical homogeneity in interfacial compositions and preservation

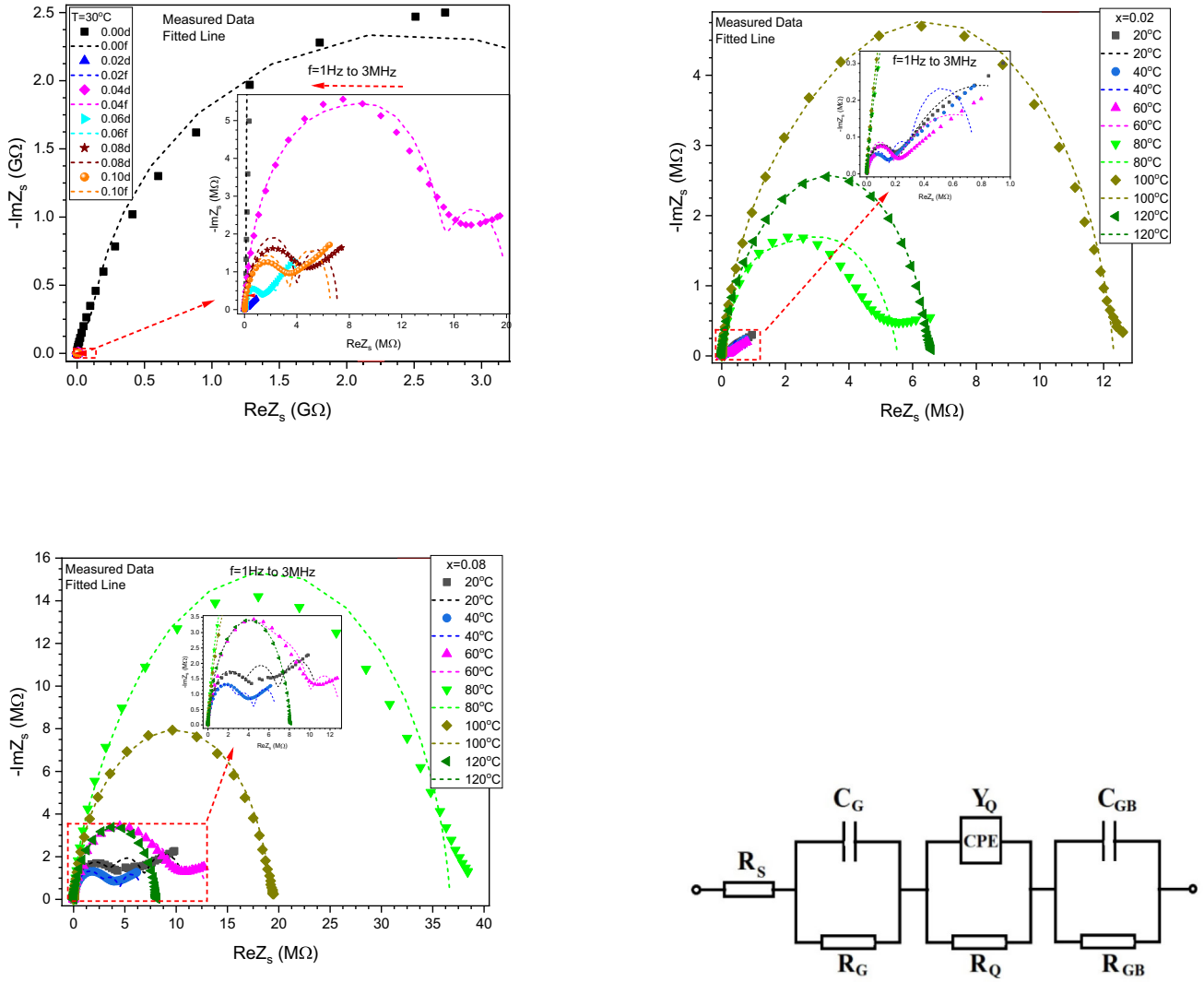

Fig. 18 Nyquist fitting plots of the Cole–Cole complex impedance function for **(a)** T = 300 °C (x varies) **(b)** x = 0.02 (T varies) **(c)** x = 0.08 (T varies) and **(d)** equivalent electrical circuits of the fitted model R(CR)(QR)(CR) for the Ag → CoNiZnCu (x ≤ 0.10) NSFs

Table 5 Dependence of substitution on equivalent-circuit fitting parameters for Ag → CoNiZnCu (x ≤ 0.10) NSFs at T = 30 °C with different Ag^{+} ion substitution ratios (x = 0.00–0.10)

x →	0.00	0.02	0.04	0.06	0.08	0.10
R_S (Ω)	1.6G	3 m	0	8	0	0
C_G (F)	27n	∞	306n	62µ	382	306n
R_G (Ω)	0	∞	0.02	32G	∞	0.734
CPE Yo ($S{\cdot}s^n$)	398p	8n	639n	114p	98p	621µ
CPE exponent n	0.00	0.61	0.90	0.85	0.86	0.24
R_Q (Ω)	∞	635 k	16 M	1.7 M	5.9 M	9.7G
C_{GB} (F)	68n	992 m	457µ	9n	0	∞
R_{GB} (Ω)	282 M	0	9.7G	2.1 M	0	62 k

Table 6 Temperature dependence of equivalent-circuit fitting parameters for the Ag → CoNiZnCu ($x \leq 0.10$) NSFs with $x = 0.02$, measured between 20 and 120 °C

Temp. (°C) →	20	40	60	80	100	120
R_S (Ω)	0.7	1.2	0	792	1.9	0.6
C_G (F)	221n	34n	∞	23p	29p	1.4μ
R_G (Ω)	4.3G	471 k	132	5 M	10 M	1.6 M
CPE Yo ($S{\cdot}s^n$)	1.4n	761p	673p	15 m	72n	122p
CPE exponent n	0.73	0.78	0.78	177n	0.53	0.88
R_Q (Ω)	453 k	199 k	264 k	9.7G	128 M	6.5 M
C_{GB} (F)	47μ	132μ	629μ	1.4μ	6.3μ	∞
R_{GB} (Ω)	16 m	238 m	407 k	0	4.6 M	1.8 M

Table 7 Temperature dependence of equivalent-circuit fitting parameters for the Ag → CoNiZnCu ($x \leq 0.10$) NSFs with $x = 0.08$, measured between 20 and 120 °C

Temp. (°C) →	20	40	60	80	100	120
R_S (Ω)	508	397 m	508	845	518 m	22.5
C_G (F)	14.3p	58μ	57n	∞	201p	1.1μ
R_G (Ω)	7.4 M	4.6 k	3.6 M	43 T	2.0	22G
CPE Yo ($S{\cdot}s^n$)	85p	78p	168n	7μ	46p	53p
CPE exponent n	0	0.88	0.49	0.95	0.91	0.90
R_Q (Ω)	575	3.6 M	10 k	0	19 M	8 M
C_{GB} (F)	27 m	4.9n	15p	14p	50μ	319 m
R_{GB} (Ω)	26 T	2.4 M	9.8 M	35 M	42 T	239 m

of semiconductor properties. Furthermore, the temperature-dependency analysis of complex impedance further confirms a thermally activated conduction mechanism. With increasing temperature from 20 °C up to 120 °C, the progressive shrinkage of semicircular arcs designates a significant reduction in both grain and grain-boundary resistances due to enhanced charge-carrier mobility. Simultaneously, the improvement in capacitance and evolution of the CPE exponent suggest activation of interfacial polarization and increased participation of localized charge carriers. In particular, the electrical trend is well explained by the coupled MW interfacial polarization mechanism and small polaron hopping conduction characteristic of NSF systems. The addition of Ag + ions effectively regulates grain-to-grain boundary interactions, reduces interfacial resistance barriers, and enhances charge-transport dynamics.

Consequently, the EEC modeling reveals that Ag^+ ion substitution provides an effective way to shape impedance properties by balancing volumetric and interfacial contributions. This tunable electrical response makes Ag → CoNiZnCu NSFs promising candidates for high-frequency electronic devices, sensors, and energy-related applications requiring stable and controllable dielectric behavior.

4 Conclusion

The Ag-substituted CoNiZnCu ($x \leq 0.10$) NSFs have been synthesized via a one-pot sol–gel combustion route. XRD analysis verified that a cubic spinel structure had formed for all composition. The surface morphology and microstructural investigation were performed using SEM and HR-TEM analysis, revealing the nanostructures with agglomeration in spherical shapes and high porosity. It was found that the lattice constant and crystalline size were observed to be in the range of 8.339–8.371 Å and 21–44 nm. In this work, the electrical and dielectric properties of Ag-substituted Ag → CoNiZnCu ($x \leq 0.10$) NSFs were systematically investigated through a multifaceted impedance spectroscopy analysis. The collective evidence provides a unified and self-consistent model where the electrical response is governed by a thermally activated electron-hopping mechanism operating within a heterogeneous microstructure of conductive grains and more resistive grain boundaries.

The findings of this study indicate that the use of Ag^+ ions in place of another cation to alter grain boundary properties was the most important contributor to the ability of cation substitution to dramatically improve D.C. conductivity. The presence of Ag^+ ions was determined to lower the resistance of grain boundaries significantly, resulting in an increase of DC conductivity by multiple orders. The increased charge carrier mobility contributes to enhanced

microwave interfacial polarization, which in turn accounts for the gigantic permittivity and very large dielectric relaxation peaks evidenced in substituted nanostructured ferrites. Complementary analytic formalisms were used to verify this model. The Nyquist plots for impedance and electric modulus provided visual confirmation of the separate electrical responses of the individual grains and the interfaces, which was not able to be accomplished using the unsubstituted NSF that contains mostly grain boundary material. This research provides evidence to support the premise that the unique electrical and dielectric characteristics of this complex ferrite result from its heterogeneity at the microstructure level. Additionally, through selective chemical substitution, these characteristics may be modified in a controlled and predictable manner.

Acknowledgements The authors acknowledge the financial support provided by the Research, Development, and Innovation Authority (RDIA), Saudi Arabia, Riyadh, under the 'Reactivating & Rebuilding of Existing Labs Initiative' (Grant No. 12959-iau-2023-iau-R-3-1-SE), which supported the generation of TEM images. Prof. A. Baykal acknowledges Istanbul Aydin University Project Support Center with the project number of İAÜ BAP 2026-3.

Funding Open access funding provided by the Scientific and Technological Research Council of Türkiye (TÜBİTAK).

Declarations

Conflict of interest The authors declare that they have no known competing financial interests or personal relationships that could have appeared to influence the work reported in this paper. The authors declare the following financial interests/personal relationships, which may be considered as potential competing interests.

References

1. Prabagar, C.J.; Anand, S.; Janifer, M.A.; Pauline, S.; Theoder, P.A.S.: Effect of metal substitution (Zn, Cu and Ag) in cobalt ferrite nanocrystallites for antibacterial activities. Mater. Today Proc. **47**, 1999 (2021)
2. Kadam, S.S.; More, V.D.; Patil, M.R.; Shirsath, S.E.; Fulari, A.V.; Shinde, V.S.; Kammar, S.S.; Kadam, R.H.; Kadam, A.B.: Crystallographic and magnetic modulation via Sm^{3+}-driven cation rearrangement in Co-Cr spinel ferrite nanoparticles for magnetic device applications. J. Magn. Magn. Mater. **630**, 173420 (2025)
3. Aziz, C.: Effects of grinding technique and Dy^{3+} doping on optical and impedance properties of cobalt ferrites synthesized by the solgel autocombustion method. Ceram. Int. **52**, 217 (2026)
4. Aydi, S.; Garoui, I.; Nasri, S.; Akermi, M.; Djebali, R.; Oueslati, A.: Engineering spinel ferrites via A-site cation substitution: structural, electrical, and optical properties for advanced applications. Ceram. Int. **51**, 48861 (2025)
5. Salih, S.J.; Tahseen, Z.S.: Spinel ferrite nanoparticles in environmental remediation: adsorption, catalysis, and sustainability perspectives. Next Sustainability **7**, 100240 (2026)
6. Salih, S.J.; Mahmood, W.M.: Review on magnetic spinel ferrite (MFe_2O_4) nanoparticles: from synthesis to application. Heliyon **9**, e16601 (2023)
7. Aepurwar, D.N.; Shirsath, S.E.; Batoo, K.M.; Hadi, M.; Devmunde, B.H.: Effect of Li^+ ion on the physico-chemical properties cation distribution of sol-gel synthesized Ni-Zn spinel ferrite nanoparticles. Ceram. Int. **50**, 55658 (2024)
8. Humbe, A.V.; Kounsalye, J.S.; Somvanshi, S.B.; Kumar, A.; Jadhav, K.M.: Cation distribution, magnetic and hyperfine interaction studies of Ni–Zn spinel ferrites: role of Jahn Teller ion (Cu^{2+}) substitution. Mater. Adv. **1**(4), 880 (2020)
9. Hashim, M.; Ismail, M.M.; Batoo, K.M.; Hadi, M.; Salih, S.J.; Meena, S.S.; Jotania, R.B.; Kumar, N.P.; Naidu, K.C.B.; Shirsath, S.E.: Structural, optical, and dielectric properties of $Co_{0.6}Mn_{0.4}Gd_xFe_{2-x}O_4$ ferrites prepared through sonochemical method. Ceram. Int. **50**, 42677 (2024)
10. Sowjany, P.; Thirupathi, G.; Kumar, M.S.; Ramesh, T.; Reddy, M.V.R.; Chelvane, A.; Kumar, N.P.: Comparison of structural, optical, electrical and magnetic properties between $Ni_{0.5}Co_{0.5}Gd_{0.005}Tb_{0.005}Fe_{1.99}O_4$ and $Ni_{0.5}Co_{0.5}Gd_{0.0033}Tb_{0.0033}Dy_{0.0033}Fe_{1.99}O_4$. J. Alloys Compd. **971**, 172623 (2024)
11. Coury, F.G.; Zepon, G.; Bolfarini, C.: Multi-principal element alloys from the CrCoNi family: outlook and perspectives. J. Mater. Res. Technol. **15**, 3461 (2021)
12. Harisha, G.; Devaraja, C.; Thejas, R.; Murugendrappa, M.V.; Rajashekara, K.M.; Kaewkhao, J.; Rajaramakrishna, R.: Exploration of structural and morphological characteristics of Ag^{2+} substituted Zn-$CuFe_2O_4$ nanoparticles by green synthesis. Nano-Struct. Nano-Objects **36**, 101058 (2023)
13. Okba, E.A.; Fakhry, F.E.; El-Bahnasawy, H.H.; Abdel-Galeil, M.M.; El Shater, R.E.: Development of heterogeneous photocatalysis delafossite structured Ag doped Cd-Cu ferrite spinel nanoparticles for an efficient photodegradation process. J. Photochem. Photobiol. A Chem. **448**, 115275 (2024)
14. Fei, D.; Guo, Y.; Zhou, J.; Tao, J.; Chen, N.; Yao, Z.; Tao, X.; Duan, L.; Liu, J.; Ouyang, B.: Chemical silver plating synergistically enhances the contribution of interfaces and defects in the Ni-Zn-Nd spinel ferrite-based electromagnetic wave absorbing material. Mater. Res. Bull. **173**, 112662 (2024)
15. Mangood, A.H.; Gemeay, A.H.; Abdel-Galeil, M.M.; Salama, E.S.; El-Shater, R.E.: Evaluation of synergistic approach of spinel cadmium–copper nanoferrites as magnetic catalysts for promoting wastewater decontamination: Impact of Ag ions doping. Environ. Sci. Pollut. Res. **30**, 106876 (2023)
16. Tamboli, Q.Y.; Bushnak, I.; Patange, S.M.: Effect of Ag on dielectric, elastic, electrical impedance and Raman spectroscopic properties of $CoFe_2O_4$. J. Sol-Gel Sci. Technol. **116**, 114 (2025)
17. Satheeshkumar, M.K.; Kumar, E.R.; Srinivas, C.; Suriyanarayanan, N.; Deepty, M.; Prajapat, C.L.; Rao, T.V.C.; Sastry, D.L.: Study of structural, morphological and magnetic properties of Ag substituted cobalt ferrite nanoparticles prepared by honey assisted combustion method and evaluation of their antibacterial activity. J. Magn. Magn. Mater. **469**, 691 (2019)
18. Rathod, S.M.; Chavan, A.R.; Jadhav, S.S.; Batoo, K.M.; Hadi, M.; Raslan, E.H.: Ag^+ ion substituted $CuFe_2O_4$ nanoparticles: Analysis

of structural and magnetic behavior. Chem. Phys. Lett. **765**, 138308 (2021)
19. Alshahrani, B.; ElSaeedy, H.I.; Fares, S.; Korna, A.H.; Yakout, H.A.; Ashour, A.H.; Fahim, R.A.; Kodous, A.S.; Gobara, M.; Abdel Maksoud, M.I.A.: Structural, optical, and magnetic properties of nanostructured Ag-substituted Co-Zn ferrites: insights on anticancer and antiproliferative activities. J. Mater. Sci. Mater. Electron. **32**, 12383 (2021)
20. Soudani, I.; Almutairi, F.N.; Chaabane, I.; Oueslati, A.; Aydi, A.; Khirouni, K.: Conduction mechanism and dielectric relaxation in $LiMg_{0.5}Fe_2O_4$ spinel ferrite: a temperature- and frequency-dependent complex impedance study. J. Phys. Chem. Solids **201**, 112631 (2025)
21. Almessiere, M.A.; Ünal, B.; Baykal, A.; Mojtahedi, E.; Mihmanlı, A.; Kahraman, S.: Defect-engineered charge transport and dielectric relaxation in In/Se co-substituted CoNi spinel ferrite nanoparticles by sonochemical route. Mater. Sci. Eng., B **325**, 119138 (2026)
22. M.A. Almessiere, A. Baykal, S.E. Shirsath, M.A. Gondal, Md Amir, Y. Slimani, Role of Al^{3+} ion substitution in modulating conductivity and interfacial polarization in CoNiCuZn spinel ferrite: Cation distribution study
23. Murthy, P.K.; Kiran, K.S.; Melagiriyappa, E.; Veena, M.: Investigation of Cd^{2+} and Nd^{3+} ions substitution on the structural, morphological dielectric and impedance properties of $Ni_xCd_{1-x}Nd_yFe_{2-y}O_4$ ($0 \leq x \leq 1.0$) spinel ferrites nanoferrites for high-frequency applications. J. Alloys Compd. Commun. **8**, 100139 (2025)
24. Ashiq, M.G.B.: Dielectric, impedance and electric modulus properties of lanthanum-doped zinc spinel ferrite ($ZnLa_xFe_{2-x}O_4$) nanomaterials. Ceram. Int. **51**, 52989 (2025)
25. Rani, P.; Verma, N.; Godara, P.; Singh, R.M.: Complex impedance spectroscopic analysis of charge transport and relaxation mechanism in Co0.5Cu0.5Fe2O4 nano ferrites. Mater. Sci. Eng., B **313**, 117954 (2025)
26. Routray, K.L.; Saha, S.; Behera, D.: Insight into the anomalous electrical behavior, dielectric and magnetic study of Ag-doped $CoFe_2O_4$ synthesised by Okra extract-assisted green synthesis. J. Electron. Mater. **49**(12), 506 (2020)
27. Saha, S.; Routray, K.L.; Hota, P.; Dash, B.; Yoshimura, S.; Ratha, S.; Nayak, T.K.: Structural, magnetic and dielectric properties of green synthesized Ag doped $NiFe_2O_4$ spinel ferrite. J. Mol. Struct. **1302**, 137409 (2024)
28. Alshahrani, B.; ElSaeedy, H.I.; Fares, S.; Korna, A.H.; Yakout, H.A.; Ashour, A.H.; Fahim, R.A.; Kodous, A.S.; Gobara, M.; Abdel Maksoud, M.I.A.: Structural, optical, and magnetic properties of nanostructured Ag-substituted Co-Zn ferrites: insights on anticancer and antiproliferative activities. J. Mater. Sci. Mater. Electron. **32**(9), 12383 (2021)
29. Ren, K.; Ma, R.; Wang, Z.; Qin, S.; Chen, R.; Ma, X.; Ma, P.; Li, S.; Xie, Z.; Yao, X.; Lu, F.: Grain size dependence of TiZrNbV spallation and impact-energy-release behavior. Int. J. Mech. Sci. **293**, 110164 (2025)
30. Ferreira, L.S.; Silva, T.R.; Silva, V.D.; Raimundo, R.A.; Simões, T.A.; Loureiro, F.J.; Fagg, D.P.; Morales, M.A.; Macedo, D.A.: Spinel ferrite MFe_2O_4 (M = Ni, Co, or Cu) nanoparticles prepared by a proteic sol-gel route for oxygen evolution reaction. Adv. Powder Technol. **33**, 103391 (2022)
31. Almessiere, M.A.; Baykal, A.; Shirsath, S.E.; Gondal, M.A.; Amir, M.; Slimani, Y.: Role of Al^{3+} ion substitution in modulating conductivity and interfacial polarization in CoNiCuZn spinel ferrite: cation distribution study. Nano-Struct. Nano-Objects **44**, 101566 (2025)
32. Kadam, S.S.; More, V.D.; Patil, M.R.; Shirsath, S.E.; Fulari, A.V.; Shinde, V.S.; Kammar, S.S.; Kadam, R.H.; Kadam, A.B.: Crystallographic and magnetic modulation via Sm^{3+} - driven cation rearrangement in Co-Cr spinel ferrite nanoparticles for magnetic device applications. J. Magn. Magn. Mater. **630**, 173420 (2025)
33. Patil, A.A.; Gaikwad, V.P.; Phase, R.H.; Kadam, S.E.; Shirsath, J.J.: Chamargore, Rare earth Ce and Y cation co-substitution and its effects on the strain, elasticity, and magnetism of Co-Zn ferrite nanomaterials. Ceram. Int. **51**, 21675 (2025)
34. Li, Z.; Jin, X.; Hu, C.; Dai, B.; Ren, Y.; Xu, F.; Zhao, Y.; Yuan, X.: Effects of thermal, stress, and electric fields on microstructure and ion distribution of $(Mg_{0.1}Mn_{0.1}Co_{0.1}Ni_{0.2}Ti_{0.1}Cu_{0.1}Zn_{0.2})Fe_{2.1}O_4$ spinel ferrites. Ceram. Int. **50**, 20260 (2024)
35. Soufi, A.; Hajjaoui, H.; Elmoubarki, R.; Abdennouri, M.; Qourzal, S.; Barka, N.: Spinel ferrites nanoparticles: synthesis methods and application in heterogeneous Fenton oxidation of organic pollutants–a review. Appl. Surf. Sci. Adv. **6**, 100145 (2021)
36. Rajenimbalkar, R.S.; Deshmukh, V.J.; Patankar, K.K.; Somvanshi, S.B.: Effect of multivalent ion doping on magnetic, electrical, and dielectric properties of nickel ferrite nanoparticles. Sci. Rep. **14**, 29547 (2024)
37. Ünal, B.; Baykal, A.; Almessiere, M.A.; Mihmanlı, A.: A. Influence of temperature and selenium substitution on electrical and dielectric characteristics of $CoFe_2O_4$ nanoparticles. J. Indian Chem. Soc. **102**, 101620 (2025)
38. Routray, K.L.; Saha, K.S.; Behera, D.: Insight into the anomalous electrical behavior, dielectric and magnetic study of Ag-substituted $CoFe_2O_4$ synthesized by Okra extract-assisted green synthesis. J. Electron. Mater. **49**, 7244 (2020)
39. Slimani, Y.; Ünal, B.; Almessiere, M.A.; Demir-Korkmaz, A.; Shirsath, S.E.; Yasine, G.; Trukhanov, A.V.; Baykal, A.: Investigation of structural and physical properties of Eu^{3+} ions substituted $Ni_{0.4}Cu_{0.2}Zn_{0.4}Fe_2O_4$ spinel ferrite nanoparticles prepared via sonochemical approach. Results Phys. **17**, 103061 (2020)
40. Almessiere, M.A.; Ünal, B.; Demir Korkmaz, A.; Shirsath, S.E.; Baykal, A.; Slimani, Y.; Gondal, M.A.; Baig, U.; Trukhanov, A.V.: Electrical and dielectric properties of rare earth substituted hard-soft ferrite $(Co_{0.5}Ni_{0.5}Ga_{0.01}Gd_{0.01}Fe_{1.98}O_4)_x/(ZnFe_2O_4)_y$ nanocomposites. J. Mater. Res. Technol. **15**, 969 (2021)
41. Ponpandian, N.; Narayanasamy, A.: Influence of grain size and structural changes on the electrical properties of nanocrystalline zinc ferrite. J. Appl. Phys. **92**, 2770–2778 (2002). https://doi.org/10.1063/1.1498883
42. Lia, Q.; Liua, X.; Wang, H.; Lan, Z.; Zhang, K.; Wua, C.; Liu, P.; Jianga, X.; Sun, K.; Yu, Z.; Grain-boundary-engineered MnZn ferrites with suppressed power loss and enhanced temperature stability. Ceram. Int. **51**, 20813–20821 (2025)
43. Wang, F.; Sun, C.; Yin, X.; Yang, Y.; Yu, N.; Li, Y.; Li, Y.: Investigation on electromigration failure mechanism and lifetime prediction of interconnects under multifield coupling for chiplet applications. IEEE Trans. Electron Devices **73**, 552 (2026)
44. Yang, G.; Zhou, S.; Xiao, J.; Zhang, H.; Yang, J.L.: Effect of materials with different permittivity on the sensing depth of open-ended coaxial probes at different frequencies. Rev. Sci. Instrum. **96**, 104711 (2025)
45. Ganesh, M.; Mohapatra, P.; Jain, A.; Aich, S.; Dobbidi, P.: Unveiling the potential of Dy+3 substituted Ni-Zn ferrites: A study of physical, magnetic, dielectric, and microwave properties. Materialia **33**, 101990 (2024)
46. Li, X.; Jin, T.; Wang, Z.; Chen, Y.; Yun, C.; Shang, J.; Ge, Y.; Lu, T.; Zhuang, W.; Ma, Y.; Qi, Z.: Hydroxyl-rich hyperbranched polyglycerol additive for low-temperature aqueous zinc batteries: sustained and efficient dehydration and high-conductivity. Adv. Sci. **13**, e16639 (2026)